AN ABSTRACT OF THE THESIS OF

Thomas B. Swanson for the degree of Doctor of Philosophy in Physics presented on July 11, 1995. Title: A Rubidium Atomic Funnel.

Redacted for Privacy

Abstract Approved: _____
David H. McIntyre

A low velocity, low temperature beam of atoms is produced from a two-dimensional magneto-optic trap known as an atomic funnel. The funnel provides simultaneous spatial and velocity compression of atoms and will provide a source for a three-grating atomic interferometer. Rubidium atoms from an oven are slowed by chirped cooling and loaded into the trap. Atoms are ejected from the trap using frequency offsets in optical molasses. The resultant beam has a controllable velocity in the range of 3 to 10 m/s with temperatures of order 500 μK.

A Rubidium Atomic Funnel

by

Thomas B. Swanson

A THESIS

submitted to

Oregon State University

in partial fulfillment of

the requirements for the

degree of

Doctor of Philosophy

Completed July 11, 1995

Commencement June 1996

Doctor of Philosophy thesis of Thomas B. Swanson presented on July 11, 1995

APPROVED:

Redacted for Privacy

Major Professor, representing Physics

Redacted for Privacy

Chair of Department of Physics

Redacted for Privacy

Dean of Graduate School

I understand that my thesis will become part of the permanent collection of Oregon State University libraries. My signature below authorizes release of my thesis to any reader upon request.

Redacted for Privacy

Thomas B. Swanson, Author

Acknowledgments

First and foremost I would like to thank my thesis advisor, David McIntyre, for his help with this work, for seeming to know virtually everything on any topic I happened to broach and for having the impeccable timing of arriving in Corvallis and starting up his research group in an interesting subject at the same time I arrived and was looking to begin research.

The thanks and blame for convincing me to go to grad school and, more importantly, to stay and complete my Ph.D. go to Gilberto Barreto and Naren Shankar. Gil would have been proud. This isn't soccer camp.

The combination of completing this project and surviving graduate school were not done on my own. There are many people to thank who have worked on the various projects necessary to start up the lab, to get equipment built and fixed and for the actual running of the experimental apparatus. Thanks go to:

Chris Cuneo for his friendship, his help both in and out of the lab and for running interference for me when I needed it.

Nancy Silva for her tremendous amount of help in the last eighteen-or-so months in getting this experiment to work.

Corinne (Carmine) Grande, Shannon Mayer and a cast of several for their contributions to the lab both past and present, and to Jeff Gruen for being the low man on the totem pole and not seeming to mind.

Jeff Maki for his contributions as postdoc.

Dennis Tom for his computer expertise and procurement of interesting computer games to provide late-night diversions which were especially welcome when the experiment wasn't going well.

The basketball and card players of the Physics Department for providing two enjoyable activities to help alleviate the stress and boredom, and many other friends, whom I will not attempt to list for fear of forgetting someone.

And to Mom and Dad for supporting but not pushing.

Financial support has been provided by the Office of Naval Research, Department of Education and Oregon State University.

Table of Contents

Table of Contents (Continued)

Page

List of Figures

Figure Page

List of Figures (Continued)

Figure Page

List of Appendix Figures

Figure Page

A Rubidium Atomic Funnel

Chapter 1
Introduction

The ability to manipulate neutral atomic beams in much the same manner as optical beams has become a reality in recent years. This new field of atom optics has emerged with the introduction of laser cooling and trapping techniques and advances in fabrication of material structures of sub-micron size.

There are two methods by which a laser field may exert a force on a neutral atom. The dipole force uses a strong laser field to induce a dipole moment in an atom, which then interacts with the electric field of the laser. This force is conservative and gives rise to behavior that is familiar in optics. The dipole force has been used to make mirrors [Balykin, *et al.*, 1987], gratings [Martin, *et al.*, 1988] and lenses for atoms [Bjorkholm, *et al.*, 1978].

The spontaneous or scattering force relies on (near) resonant absorption of the laser light and spontaneous emission. Each absorption and emission will change the momentum of the atom by a value equal to the photon's momentum and can, over the course of many absorption/emission cycles, exert a significant force on the atom. Induced emission causes no net force, as the direction of the absorbed and emitted photons are the same and the momentum changes cancel each other out. Laser cooling and trapping

techniques, using the dissipative spontaneous force, make it possible to build devices without optical analogues.

Atoms can be reflected [Anderson, *et al.*, 1986], diffracted [Estermann and Stern, 1930 and Keith, *et al.*, 1988] and focused [Berkhout, *et al.*, 1989, Carnal, *et al.*, 1991] with the proper material structures. Advances in microfabrication techniques allow for precision crafting of small scale structures. The technology has recently reached a point where the scale of the material structures is within a few orders of magnitude of the deBroglie wavelength of atoms. The diffraction angles resulting from atomic diffraction are large enough to be exploited in a reasonably sized vacuum system.

The demonstration of interference of atoms is a logical extension of the field of atom optics. The realization of an atomic interferometer would allow for dramatic improvement in some interferometric measurements as atoms have much smaller velocities than photons and thus have long interaction times. Interference has been demonstrated for neutrons [e.g. Werner, 1980 and Greenberger, 1983] but atoms are more practical than neutrons, since atoms are available from more convenient and brighter sources.

Given the recent advances in this field we have embarked on an effort to construct an atom interferometer using a source of slow, cold atoms and microfabricated transmission gratings. The three-grating design is similar to the x-ray interferometer of Bonse and Hart [1965], a design also used for neutron interference experiments [Bauspiess, *et al.*, 1974]. The incident atomic beam is diffracted by the first grating. The second grating is wide enough to accept two of

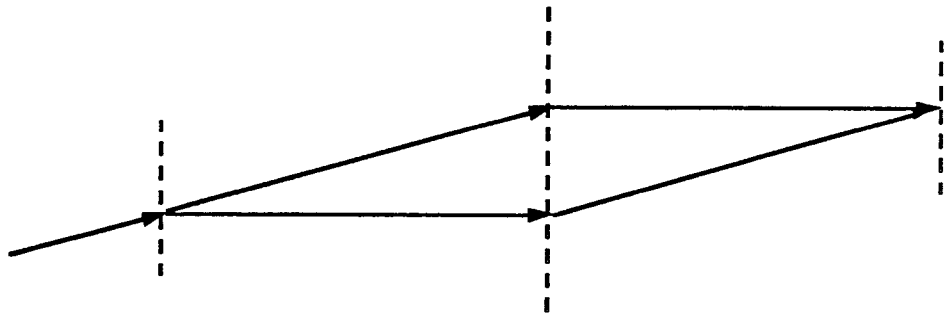

Fig. 1.1. A three grating interferometer. The incident beam is diffracted at the first grating and two of the resulting beams are diffracted by the middle grating. Two of the beams combine and interfere at the third grating.

the diffracted beams which are again diffracted. Two of these beams combine and interfere at the position of the third grating, as shown in Fig. 1.1. Due to the inherently equal path lengths of the two interfering beams, the interference is independent of the wavelength of the incident beam.

Atom Interferometry

Four different atom interferometry experiments were reported in 1991. Two experiments [Carnal and Mlynek, 1991, Keith *et al.*, 1991a] used physical structures to separate a supersonic atomic beam (He and Na, respectively) into two coherent paths and then recombine them. The small deBroglie wavelengths and hence small diffraction angles required each interferometer to be over 1 m long. The other two experiments [Riehle *et al.*, 1991, Kasevich

and Chu, 1991] used photon recoil to separate and recombine the atomic beam.

The three grating interferometer we have chosen to build will use laser cooled atoms and microfabricated transmission gratings. The longer deBroglie wavelengths of cold, slow atoms will result in larger diffraction angles and will allow for a smaller overall interferometer length of 10 cm. This will permit all three gratings to be mounted on a single chassis and reduce independent vibration that would tend to reduce contrast of the output signal.

Background

The idea of laser cooling of atoms was introduced by Hänsch and Schawlow [1975] for neutral atoms and by Wineland and Dehmelt [1975] for trapped ions. The interest in cold atoms in traps or beams was motivated, in part, by the potential for reduction of Doppler effects in high-resolution spectroscopy and investigation of ultra low energy collisions between atoms and with surfaces.

Optical molasses, a quasi-confinement by resonant radiation pressure, was first observed by Chu *et al.* [1985] with temperatures consistent with a limit based on the simple two-level model of laser cooling. The velocity-selective damping of optical molasses is dissipative and allows for phase space compression of atoms, allowing for an increase in brightness (atoms/s per velocity interval $\Delta v_{x,y,z}$). The temperature analysis of the molasses subsequently proved incomplete as even colder temperatures were reported [Lett,

et al. 1988]. New cooling mechanisms, due to the multilevel nature of the atom and polarization gradients, were subsequently explained [Dalibard, *et al.*, 1989, Chu, *et al.*, 1989].

Confinement of atoms in a three dimensional magneto-optic trap loaded from a laser cooled beam was reported by Raab, *et al.* [1987] and allowed for lengthy confinement of a large number of cold atoms. The spatial compression of the trap combined with the velocity damping of optical molasses results in a further increase in the brightness of the atoms. Trapping of atoms from a vapor rather than from a cooled beam was demonstrated by Monroe, *et al.* [1990] which allowed some cold atom experiments with much simpler apparatus than was previously necessary.

The Atomic Funnel

Simple one-dimensional laser cooling of a hot atomic beam is insufficient to produce a source for our interferometer. As the atoms' longitudinal velocity is reduced there is an increase in the transverse velocity and the resultant spatial expansion of the beam is unacceptable in terms of the atomic flux necessary for detection after passing through the interferometer. For this reason we use a two-dimensional magneto-optic trap, a so-called "atomic funnel," to produce a low velocity, low temperature atomic beam suitable for the interferometer. Other funnels have been built [Riis, *et al.*, 1990, Nellessen, *et al.*, 1990 and Yu, *et al.*, 1994] but do not possess all of the characteristics we require: these funnels either have lasers

directed along the funnel axis which would be blocked by our interferometer gratings and/or do not have simultaneous longitudinal and transverse cooling necessary for maximum brightness of the beam.

My task in this project was to produce a cold atomic beam at controllable velocities. With the interferometer gratings placed 30 cm from the funnel, velocities of order 10 m/s must be achieved to minimize the vertical drop due to gravity that might make the beam that enters the first grating miss the third grating or miss the interferometer altogether.

Scope of this Thesis

Chapter 2 presents the theory behind slowing, cooling and trapping of rubidium atoms and their behavior in the atomic funnel. Chapter 3 details the performance of the lasers and their role in the experiment. Chapter 4 discusses the physical layout and utilization of the lasers. Chapter 5 describes the vacuum system components and the oven used as the source for the hot atomic beam. Chapter 6 summarizes the operation of the system, from hot beam through cooling and trapping to the production of the cooled beam ejected from the atomic funnel. Chapter 7 describes the methods used to investigate the cold beam characteristics and presents the results of the beam characterization.

Chapter 2
Atom Manipulation by Lasers

The scattering (or spontaneous) force due to absorption and subsequent spontaneous emission of photons is the primary means of controlling the trajectory of atoms in this experiment.

A force will be exerted on a free atom due to the momentum transfer in the absorption-emission cycle. The absorption of photons from a defined direction (as with a laser) will transfer momentum to the atom. The photons emitted during de-excitation of the atom will contribute zero net momentum when averaged over several emission events since the emission distribution is symmetric. This will yield velocity and position dependent forces on the atoms when properly exploited. A very thorough review of these processes is given by Lett, *et al.* [1989].

Laser Slowing of Atoms

Consider a narrow-band laser interacting with a group of unbound two-level atoms with an electric dipole transition at angular frequency ω_0. The laser is tuned to frequency ω, below (to the red side of) the transition. Those atoms moving with a velocity component toward the laser will be Doppler shifted towards resonance and will scatter the incident radiation at a higher rate than those atoms moving with a velocity component in the opposite

direction. Each scattering event imparts an average momentum change of $\hbar k = h/\lambda$ to the atom, where k is the wave vector for the photon. The recoil velocity is thus

$$v_R = \hbar k/M \tag{2.1}$$

for an average scattering event where M is the atomic mass. For ^{85}Rb this is a velocity change of 0.6 cm/s per absorption. Given thermal velocities on the order of 10^5 cm/s, this allows one to view atom slowing as a continuous rather than a discrete process.

The rate of atom slowing will depend on the photon scattering rate, which is a function of Γ, the spontaneous emission rate of the atoms, Δ, the laser detuning given by

$$\Delta = \omega - \omega_0, \tag{2.2}$$

and the intensity of the laser. The laser intensity I is related to the Rabi frequency Ω by

$$\frac{I}{I_0} = \frac{2\Omega^2}{\Gamma^2}, \tag{2.3}$$

where I_0 is the saturation intensity. The scattering rate for an atom at rest is

$$R = \frac{\Gamma}{2}\frac{p}{1+p}, \tag{2.4}$$

where p is the saturation parameter and is given by

$$p = \frac{I}{I_0}\frac{(\Gamma/2)^2}{(\Gamma/2)^2 + \Delta^2}. \tag{2.5}$$

The scattering rate multiplied by the average change in momentum per scatter yields the average force on an atom:

$$\vec{F} = \hbar\vec{k}\frac{\Gamma}{2}\frac{\frac{I}{I_0}}{1+\frac{I}{I_0}+\left(\frac{2\Delta}{\Gamma}\right)^2}. \tag{2.6}$$

The limiting value for the force occurs at large intensities where the transition is saturated and the atom spends, on average, half of its time in the excited state. Thus the fastest cycling time for absorption and re-emission of the transition is twice the radiative lifetime τ ($\tau = 1/\Gamma$) and gives a maximum force of $\hbar k\Gamma/2$.

An atom in motion at velocity v toward the laser will see a Doppler shifted frequency of

$$\omega' = \omega\sqrt{\frac{1+v/c}{1-v/c}} = \omega\left(1+\frac{v}{c}+\ldots\right). \tag{2.7}$$

To first order, good for non-relativistic velocities, the laser frequency is shifted to

$$\omega' = \omega - \vec{k}\cdot\vec{v}\ . \tag{2.8}$$

The scattering force now becomes velocity dependent:

$$\vec{F} = \hbar\vec{k}\frac{\Gamma}{2}\frac{\frac{I}{I_0}}{1+\frac{I}{I_0}+\left[\frac{2\left(\Delta-\vec{k}\cdot\vec{v}\right)}{\Gamma}\right]^2}. \tag{2.9}$$

A magnetic field $\vec{B}$, directed along $\vec{v}$, can be used to shift the atomic states. This will introduce an energy shift of

$$\Delta E = -\vec{\mu} \cdot \vec{B} , \qquad (2.10)$$

which gives significant splitting of all $m \neq 0$ sublevels with relatively low fields. The shift in the atomic resonance is

$$\delta_B = m_e g_e \mu_B B - m_g g_g \mu_B B , \qquad (2.11)$$

where g is the Landé g factor for the ground (g) or excited (e) state.

For atoms with multiple hyperfine ground and excited states one generally uses circularly polarized light to drive the F to $F' = F + 1$ transition, using the highest F state to approximate a two level system. Due to selection rules the atoms will cycle in the maximum $|m_F|$ state, and the frequency shift of the resonance reduces to $\delta_B = \mu_B B$. This makes the scattering force

$$\vec{F} = \hbar \vec{k} \frac{\Gamma}{2} \frac{\frac{I}{I_0}}{1 + \frac{I}{I_0} + \left[\frac{2\left(\Delta - \vec{k} \cdot \vec{v} - \mu_B B\right)}{\Gamma} \right]^2} , \qquad (2.12)$$

where $\mu_B = (2\pi)1.4$ MHz/G is the Bohr magneton.

Now consider a thermal beam of atoms with some distribution of velocities in the direction opposite to a laser detuned, as before, below the resonance ω_0. A group of these atoms will be in resonance with the laser, scatter photons and be slowed in response to the scattering force. As the velocity of the atoms changes, the resulting Doppler shift will cause the atoms to move out of resonance. From the denominator of equation (2.12) we see that one way to maintain resonance is to scan or "chirp" the laser frequency at the same rate as the slowing. This process is known as

chirped cooling and is currently the way our atomic beam is slowed. Another method is to shift the atomic levels with a spatially varying magnetic field, called Zeeman slowing.

The scattering force, being velocity dependent, is dissipative and will narrow the Maxwell-Boltzmann velocity distribution of the atoms and thus reduces the longitudinal temperature of the atoms, hence the name laser cooling for this process. The temperature limits are discussed in the next section.

Longitudinal cooling is accompanied by transverse heating due to the recoil from spontaneous emission. The rms transverse velocity of an atom after N scattering events is given by

$$v_{\perp}^2 = \frac{v_R^2}{3} N \ , \qquad (2.13)$$

which leads to transverse expansion of the beam, especially at low longitudinal velocity.

Optical Molasses

The one-dimensional force of laser slowing may be applied in three dimensions to create a highly viscous damping field [Chu, *et al.*, 1985]. Consider two counterpropagating laser beams interacting with a group of atoms. In the low intensity regime, $I \ll I_0$, the beams may be thought to act independently on the atoms and the average force on the atom is the sum of the forces from each direction:

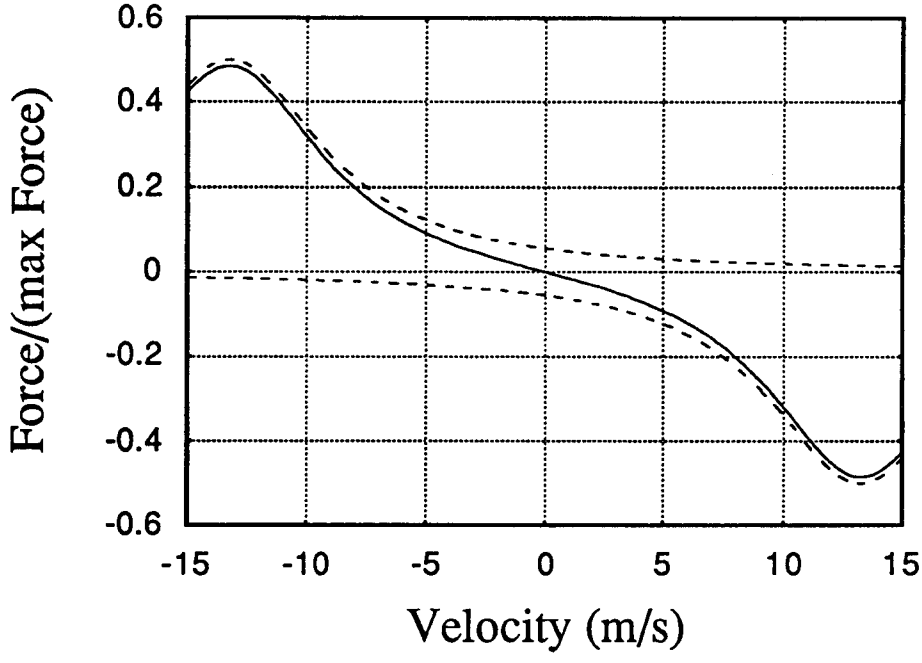

Fig. 2.1. Spontaneous force versus velocity for a detuning of -2Γ and intensity of $I = I_0/4$. The dotted lines are the individual forces from the counterpropagating lasers. For small velocities the force has the form $F = -\alpha v$.

$$F = \frac{\hbar k \Gamma}{2} \frac{I}{I_0} \frac{kv}{\Gamma} \frac{16\Delta/\Gamma}{1 + \frac{8}{\Gamma^2}\left(\Delta^2 + k^2v^2\right) + \frac{16}{\Gamma^4}\left(\Delta^2 - k^2v^2\right)^2} \quad . \qquad (2.14)$$

This force is plotted in Fig. 2.1. At low velocities, where $|kv| \ll \Gamma$ and $|kv| \ll |\Delta|$ the force is linear in v:

$$F = 4\hbar k \frac{I}{I_0} \frac{kv\left(2\Delta/\Gamma\right)}{\left[1 + \left(2\Delta/\Gamma\right)^2\right]^2} \quad . \qquad (2.15)$$

For $\Delta<0$ this is a damping or frictional force. Those atoms moving toward one laser ($\vec{k}\cdot\vec{v}<0$) will Doppler shift that laser closer to resonance so that the atom has a higher probability of absorbing a photon that opposes its motion than one directed along its motion. With the typical short (several ns) lifetime of the excited state this scenario gives rise to very large damping forces, thus the designation optical molasses. Note that the damping is with respect to the velocity; atoms will not be truly confined by the lasers.

Since the lasers providing the optical molasses are to be fixed in frequency the Doppler shift from the velocity change of a photon absorption/emission cycle must not shift the laser out of resonance. The maximum velocity change per cycle is, from equation (2.1), $2v_R = 2\hbar k/M$, so we require that $2kv_R << \Gamma$. For ^{85}Rb, $2kv_R/2\pi = 15.4$ kHz, well below the 6 MHz natural linewidth of the transition.

In analyzing the linear region we can rewrite the force in terms of a damping coefficient α such that $F = -\alpha v$:

$$\alpha = -4\hbar k^2 \frac{I}{I_0} \frac{2\Delta/\Gamma}{\left[1+(2\Delta/\Gamma)^2\right]^2} . \qquad (2.16)$$

In a region of fixed detuning the velocity will be damped as

$$v = e^{-\alpha t/M} , \qquad (2.17)$$

which gives a characteristic (1/e) damping time of $\tau_c = M/\alpha$. This has a value of ~120 μsec for $\Delta = -\Gamma$ and $I = I_0$. This damping is an average effect since it assumes the recoil due to spontaneous emission is zero. While the average velocity of the atoms can be

brought to zero, the fluctuations caused by individual spontaneous emissions means the mean-square velocity of the ensemble cannot. So the atoms will lose energy and be cooled by the dissipative force and will be heated due to the fluctuations caused by the randomness of the spontaneous emissions. The energy dissipation will cool the atoms at a rate of

$$\left(\frac{dE}{dt}\right)_{cool} = \vec{F}\cdot\vec{v} = -\alpha v^2 \cdot \qquad (2.18)$$

In a one-dimensional molasses an atom at rest is equally likely to absorb a photon from either direction. Each absorption causes the atom to undergo a random walk in momentum with step size $\hbar k$. In the one-dimensional model, where the spontaneous emission is constrained to the molasses dimension then there is a second step of equal size, giving a net $2\hbar k$. For the case of a dipole radiation pattern this factor of 2 is changed to 7/5 [Lett, *et al.*, 1989]. The mean-square momentum of the atom will increase by this factor times the square of the photon momentum. For the one dimensional case we have:

$$\frac{d\left(p^2\right)}{dt} = 2\hbar^2 k^2 R \,, \qquad (2.19)$$

where R is the total photon scattering rate. Writing the kinetic energy as $p^2/2M$ and the photon scattering rate as the sum of the positive and negative direction scattering rates, the heating is

$$\left(\frac{dE}{dt}\right)_{heat} = \frac{\hbar^2 k^2 \Gamma}{M} \frac{I/I_0}{1+\left(2\Delta/\Gamma\right)^2} \qquad (2.20)$$

in the low velocity and low intensity regime. Setting the cooling and heating rates equal we find the equilibrium mean square velocity:

$$v^2 = \frac{\hbar\Gamma}{4M}\frac{1+(2\Delta/\Gamma)^2}{2|\Delta|/\Gamma} \quad . \tag{2.21}$$

Since this represents one degree of freedom we set $k_B T/2 = Mv^2/2$:

$$k_B T = \frac{\hbar\Gamma}{4}\frac{1+(2\Delta/\Gamma)^2}{2|\Delta|/\Gamma} \quad , \tag{2.22}$$

which yields a minimum temperature, for the condition $\Delta = -\Gamma/2$, of

$$k_B T_{min} = \frac{\hbar\Gamma}{2} \quad . \tag{2.23}$$

This temperature is referred to as the Doppler cooling limit. It has a value of 140 μK for rubidium, corresponding to an rms velocity of 12 cm/s. This is well within the linear region of the scattering force, with $kv_{min}/2\pi$ = 150 kHz $<<\Gamma/2\pi$. Note also that the recoil velocity v_R is much smaller than v_{min}, which is necessary to approximate this as a continuous process.

In analyzing the molasses effects for higher intensities, the I/I_0 term in equation (2.9) is included for each laser to account for power broadening of the transition [Lett, *et al.*, 1989]. This does not account for additional cooling or heating effects that may be present due to the polarization of the lasers: if the counterpropagating lasers have the same polarization there will be a standing wave and if they have orthogonal polarizations then the lasers will drive different transitions. These effects will be discussed separately.

Polarization Gradient Cooling: A Brief Overview

The analysis of Doppler cooling ignores any effects of structure in the ground state of the atom. This structure can be important in the case where a moving atom sees different laser polarizations at different positions. These polarization gradients will force the populations of the ground state sublevels to change as the atom moves. The optical pumping necessary for this population redistribution leads to a force on the moving atom. This force can cool atoms to temperatures well below the Doppler limit and even approach the single-photon recoil limit. The two common polarization gradient possibilities are counterpropagating waves with either $\sigma^+ - \sigma^-$ polarizations or orthogonal linear polarizations.

In the case of counterpropagating waves with $\sigma^+ - \sigma^-$ polarizations, an atom at rest will see, at any point, a standing wave with linear polarization. The polarization vector has a constant magnitude and rotates through 2π each wavelength. In the case where $I \ll I_0$, each $|\pm m\rangle$ sublevel will have equal populations, with the population for a particular $|m|$ depending on the Clebsch-Gordan coefficients of the transitions.

An atom moving with a small velocity will cause a shift in the transition probabilities. This has the effect of redistributing the populations. The atoms are pumped to the state that most strongly absorbs from the laser opposing its motion which results in an increased damping force.

In the case with orthogonal linear polarizations, called $\mathrm{lin} \perp \mathrm{lin}$, the local polarization is spatially dependent, varying from

circular to elliptical to linear. The population of the |m> states depends on both the local polarization and also on the energy states, which are split because of light shifts and vary in space. At low velocities, where the time lag for optical pumping is on the order of λ/v, the light field will pump atoms from the higher energy sublevels into the low energy sublevels, so the atom radiates more energy than it has absorbed. Thus the atom spends its time always climbing a potential hill, so this effect has been called the Sisyphus effect.

A thorough treatment of these effects can be seen in Dalibard and Cohen-Tannoudji [1989].

The Magneto-Optic Trap

In order for atoms to be confined to a region of space a spatially dependent term must be present in the restoring force. One way that this may be achieved is by applying a linearly varying magnetic field to the optical molasses region. Consider the simple case of a one-dimensional trap and an atom with a $J = 0$ ($m_j = 0$) ground state and a $J' = 1$ ($m_{j'} = -1,0,+1$) excited state. The addition of a magnetic field $B = bz$ will split the atomic levels by

$$\Delta\omega = \mu_B m_j g_e B = \mu_B m_j g_e b z \,, \qquad (2.24)$$

where g_e is the Landé g factor for the excited state. The counterpropagating lasers are circularly polarized such that their angular momentum is opposed to the direction of $\vec{B}$ and are

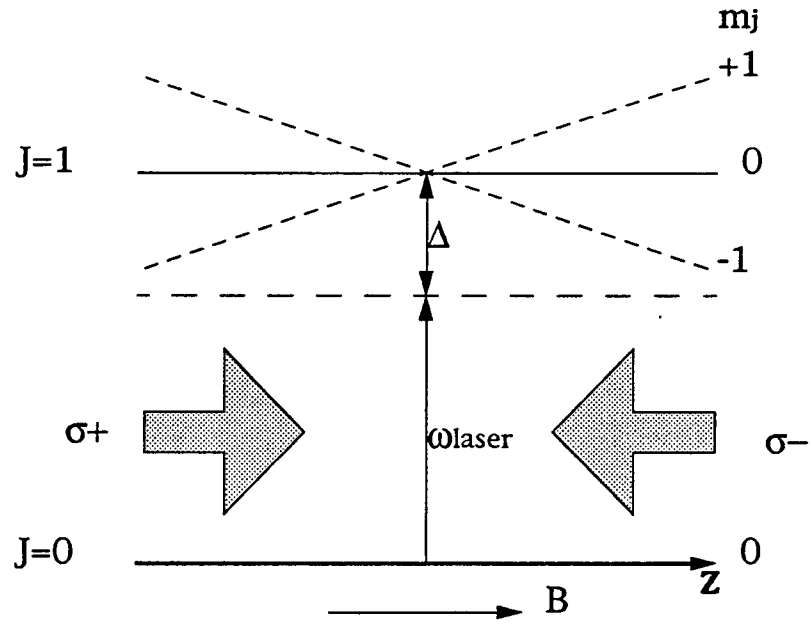

Fig. 2.2. A one-dimensional Magneto-Optic Trap. Energy level diagram shows a $J = 0$ ground state and $J' = 1$ excited state atom in a linear quadrupole magnetic field $B = bz$. The counterpropagating, circularly polarized lasers provide a restoring force to $z = 0$.

tuned, as in the molasses configuration, below the resonance frequency for $B = 0$. This configuration is depicted in Fig. 2.2.

The selection rules for electric dipole transitions dictate that m_j must change by +1 for σ^+ absorption and -1 for σ^- absorption. An atom at $z < 0$ will have the $m_{j'} = +1$ level Zeeman shifted closer to resonance and will feel a larger average force from the σ^+ laser than from the σ^- laser, giving a net force in the +z direction. Similarly an atom at $z > 0$ will feel a larger force from the σ^- laser and will also feel a restoring force to $z = 0$. The velocity damping of the optical molasses will also be present. The confinement will be present for each dimension in which there is the appropriate

magnetic field and laser polarization so confinement in two and three dimensions is possible. This configuration is known as a magneto-optic trap (MOT) or a Zeeman-shift optical trap (ZOT).

The net detuning now becomes

$$\Delta_{net} = \omega - \omega_0 - m_j g_e b z - \vec{k} \cdot \vec{v} = \Delta \pm \left(g_e b z + k v \right), \qquad (2.25)$$

where the upper (lower) sign refers to the σ^- (σ^+) beam. This can be substituted into equation (2.6) and again written as the sum of the forces of the two lasers but without restriction on intensity since each beam is exciting different transitions in the atom. Looking at low velocities and small displacements the force is

$$F = \frac{4\hbar k \frac{I}{I_0} \frac{2\Delta}{\Gamma}}{\left[1 + \frac{I}{I_0} + \left(\frac{2\Delta}{\Gamma} \right)^2 \right]^2} \left(g_e b z + k v \right). \qquad (2.26)$$

For our case of $\Delta < 0$ the linear region takes the form of a damped harmonic force: $F = -\kappa z - \alpha v$.

The capture velocity of a MOT, v_c, can be estimated in terms of the laser detuning and beam size. Monroe, *et al.* [1990] estimated the capture range as $v_c = 2\Gamma\lambda$ assuming a typical detuning of $-\Gamma$. This estimate has no dependence on trap size and would seem to underestimate v_c since significant forces can be present several linewidths away from resonance. Another method [Steane, *et al.* 1992] is to assume an atom will be trapped if it can be brought to rest in a distance equal to the trap radius, r, with one half the maximum scattering force, or, in terms of the acceleration, a,

$$v_c = \sqrt{2ar} = \sqrt{\frac{\hbar k \Gamma r}{4M}}, \qquad (2.27)$$

assuming $I/I_0 = 1$. There is no explicit dependence on detuning but this estimate can only be valid for situations where the atom can see a significant scattering force. This will be true if Δ_{net}, from equation (2.25), meets the condition $|\Delta_{net}| < \sim 2\Gamma$ at the trap boundary. This will ensure the atom will experience sufficient forces to slow it in the trap.

Optical Pumping

In the previous analysis it was assumed that the lasers drove a simple two-level atomic system with magnetic sublevels. In reality, the hyperfine splitting produces multiple ground and excited states and ensures that use of a single laser will fail to slow or trap atoms due to optical pumping. In ^{85}Rb the ground state hyperfine splitting is ~3 GHz while the excited state splitting between the $F' = 3$ and $F' = 4$ states is ~120 MHz, as shown in Fig. 2.3. A laser tuned to the closed cycle transition of $F = 3$ to $F' = 4$ will occasionally excite the $F = 3$ to $F' = 3$ transition which may then result in decay to the $F = 2$ ground state. The large ground state separation ensures that those atoms with population in the $F = 2$ ground state will be too far off resonance to interact with the laser. Because of the large number of absorptions required to slow, cool and trap atoms this ensures that essentially all atoms will be pumped into this inaccessible or "dark" state.

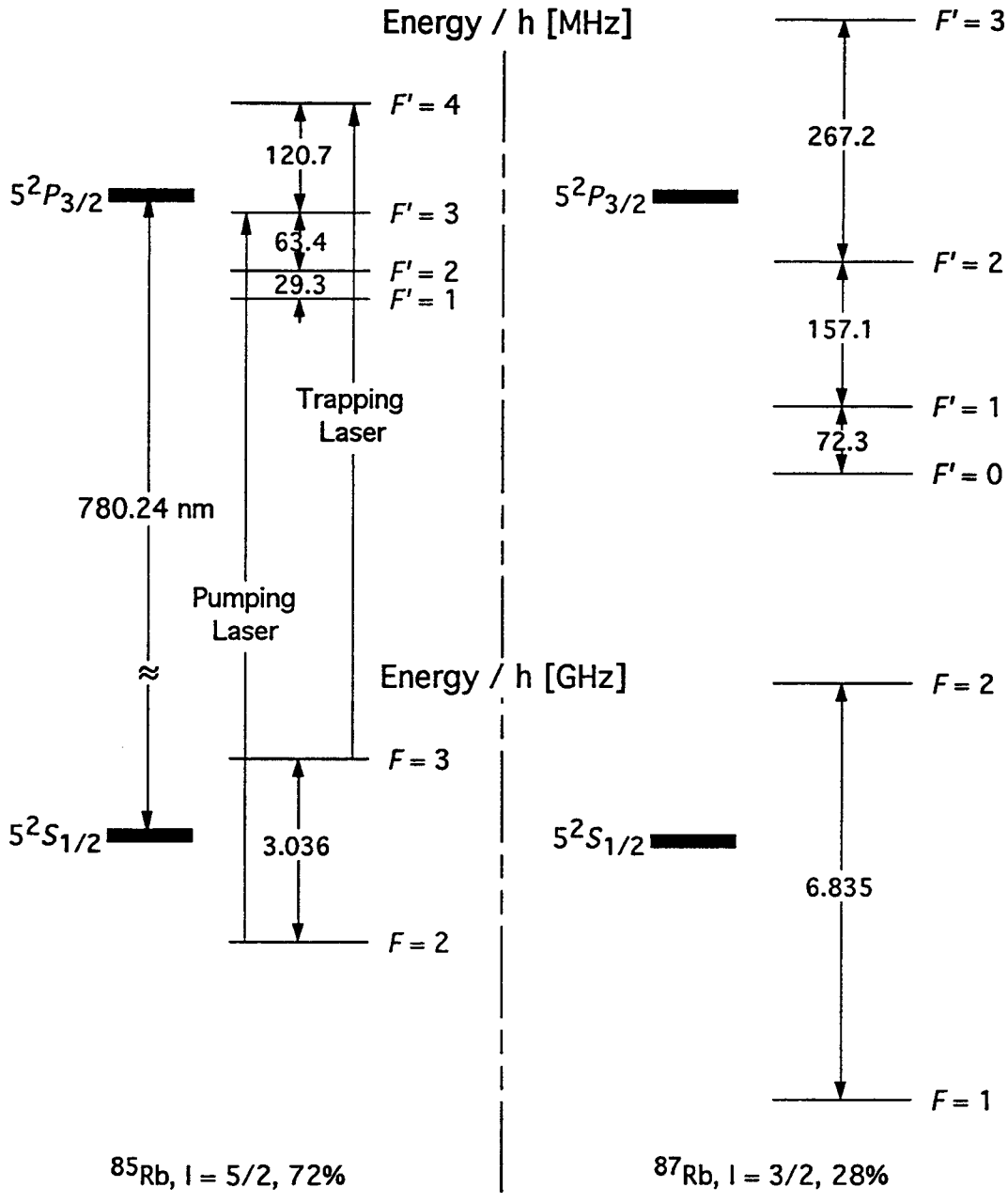

Fig 2.3. Energy level diagram showing the hyperfine structure of ^{85}Rb and ^{87}Rb. Note the different scales for ground state vs. excited state splitting. Values taken from Sheehy, *et al.* [1989].

One solution to this problem, presently used in this experiment, is to tune a second laser to the $F = 2$ to $F' = 3$ transition to optically pump the atoms back into the cycling transition. An atom in the $F' = 3$ state can return to the $F = 3$ state and once again interact with the slowing/cooling/trapping laser. For chirped cooling this laser must be synchronized with the cooling chirp to stay on resonance.

Another solution, used in the case of Zeeman slowing, is to introduce a large bias field to split the magnetic states. Circularly polarized light is used to cycle in the maximum $|m_F|$ sublevels and the level splitting from the large bias field ensures no transitions to optically pump the atoms into a "dark" state.

The Atomic Funnel

Simply laser cooling a hot atomic beam will not work in our proposed interferometer. The interferometer gratings would have to lie along the same axis as the cooling lasers, which would block the lasers, and the transverse heating and spreading present during the one-dimensional slowing would considerably reduce the brightness of the source. What is necessary is two-dimensional confinement and cooling of the beam with laser orientation that is not on the atomic beam axis.

The atomic funnel is an example of a two-dimensional magneto-optic trap. Four parallel, infinite straight wires carrying opposing current in alternate wires will produce the appropriate

magnetic quadrupole field to confine the atoms in the two dimensions perpendicular to the wires but have no confinement along the trap axis. In reality, of course, one must use finite wires with a return path for the current. The geometry we use is similar to that of Riis, *et al.* [1990], a so-called "hairpin" configuration, which was used to produce a cold (180 μK) sodium beam. In their experiment a drift velocity was imposed on the atoms by either intensity imbalances or frequency shifts in the axial laser pair.

Since we desire to place a set of interferometer gratings and hot-wire detector along the funnel axis, a molasses/trap laser in our configuration cannot lie along this axis. We place the two pairs of lasers in the horizontal plane at 45° to the funnel axis and load the atoms from a laser cooled atomic beam at 90°, as shown in Fig. 2.4 (Mechanical details of the funnel can be found in chapter 5).

In this experiment the ejection velocity from the funnel is determined by the frequency offset of the lasers in the horizontal plane. The atoms will feel zero net force in the reference frame where the scattering rates from all lasers are equal. The laser pair in the direction of motion is shifted, with respect to the nominal detuning Δ, down an amount δ, while the opposite laser pair is shifted up an equal amount. The velocity at which the force along the funnel axis is zero occurs when the Doppler shift is equal to the frequency offset:

$$\delta = \left|\vec{k}\cdot\vec{v}\right| = \frac{1}{\sqrt{2}}kv \ , \qquad (2.28)$$

which gives a velocity of

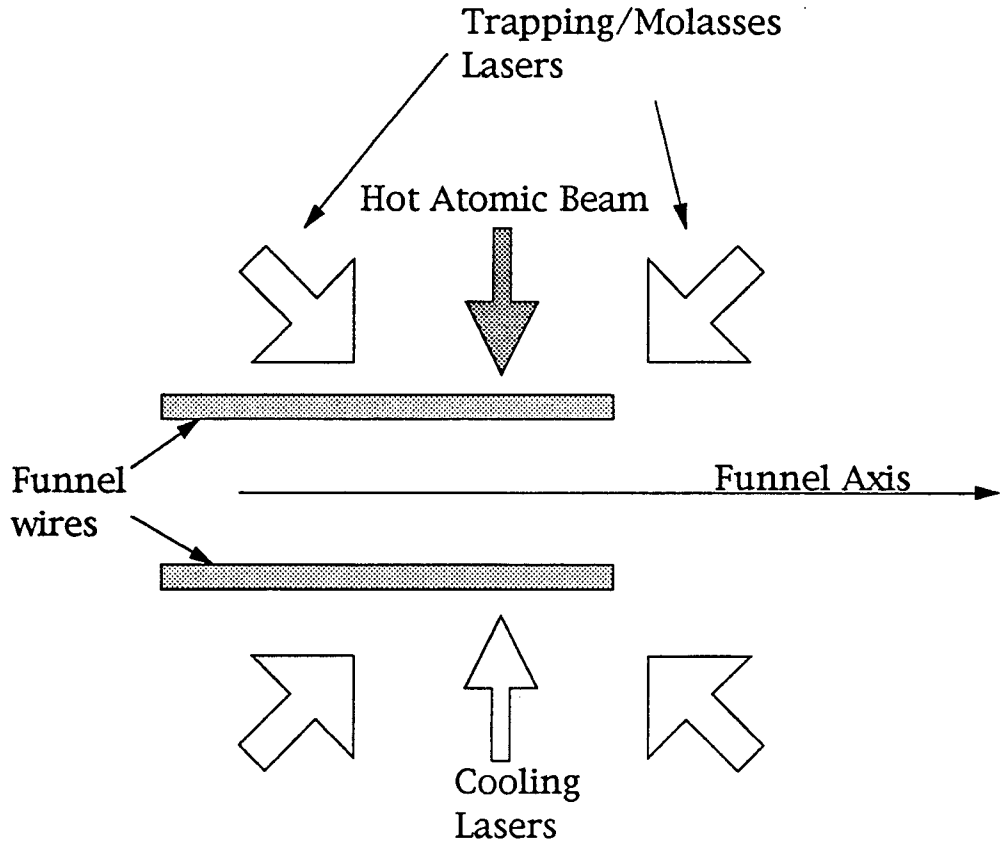

Fig 2.4. Top view of atom funnel. The horizontal lasers are 45° off axis to allow loading from the hot beam and atom ejection along the funnel axis

$$v = \sqrt{2}\frac{\delta}{k}, \tag{2.29}$$

which, for ^{85}Rb, is 1.1 m/s for a 1 MHz frequency offset.

The coordinate system of the lasers is rotated with respect to the quantization axis for the Zeeman splitting in this configuration. The circularly polarized light is now able to excite all of the m_F sublevels but does so at different probabilities such that there is still a restoring force to the $\vec{B} = 0$ line of the funnel [Delfs 1992]. The third laser, orthogonal to the 45° pairs, should be at the nominal

detuning Δ so that the moving atoms see all three beams at an equal detuning in their reference frame and improve the likelihood of orientational cooling [Riis, *et al.*, 1990].

Velocity Offsets due to Static Magnetic Fields

An axial magnetic field will cause a Zeeman shift for the atoms in the funnel which will induce a drift velocity such that the Doppler shift compensates for the Zeeman shift. Since there is no region of $\vec{B} = 0$ in this case, use of the simplistic J = 0 ground state model masks some of the subtleties of the situation. An analysis using ^{87}Rb is used since it has the appropriate properties to highlight these subtleties but has a simpler structure than ^{85}Rb. Walhout *et al.* [1992] point out that the Zeeman shift for a real atom depends on the shifts of both the ground state and excited state and that the Landé g-factors are not necessarily equal for each.

Consider an atom in a magnetic field with counterpropagating circularly polarized laser beams along the field such that the angular momentum of each beam is in the direction of propagation. In a transition from ground state (g) to excited state (e) there will be an effective detuning Δ_{eff} of

$$\Delta_{eff} = \Delta - m_e\left(kv - g_e\mu_B B\right) + m_g\left(kv - g_g\mu_B B\right), \qquad (2.30)$$

where Δ is the laser detuning given by equation (2.2). Selection rules require $\Delta m = \pm 1$. In the cases where $g_e = g_g$, this amounts to a net magnetic field shift of $\pm g_g\mu_B B$ for a transition from any of the

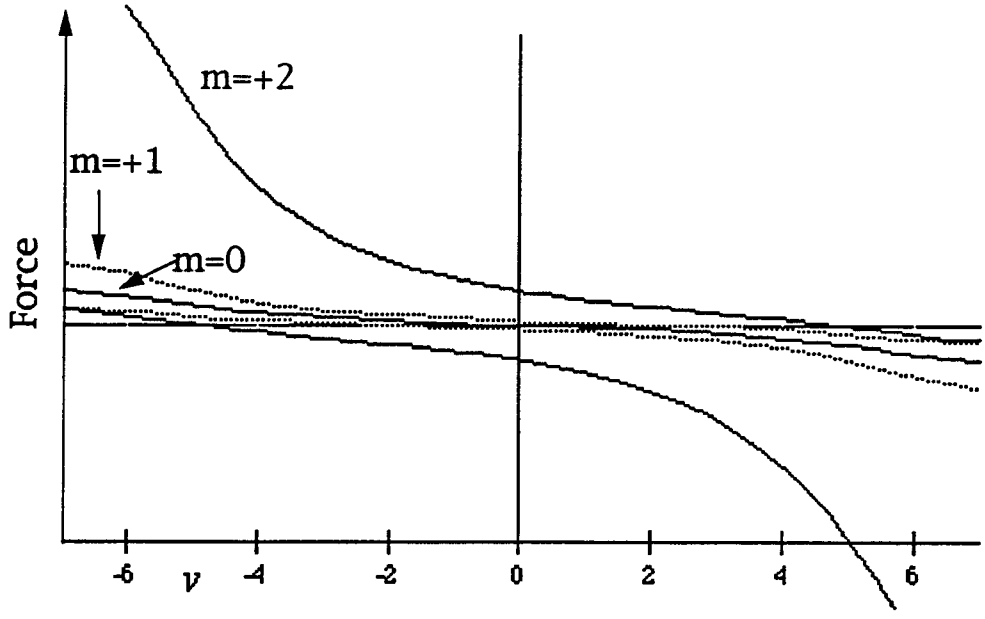

Fig. 2.5. Forces on the individual ground state |m> populations in ^{87}Rb for B = 0. Splitting from v = 0 is due to different values of the Clebsch-Gordan coefficients.

|m> sublevels of the ground state. For both isotopes of rubidium, however, $g_g < g_e$. The detuning for each transition is different so the force for each transition must be written separately and depends on the steady state population and transition probability. The average force is written as

$$F = \frac{\hbar k \Gamma}{2} \sum_{i=-F_g}^{F_g} \left[s_{i,i+1}\left(\Pi_i^g - \Pi_{i+1}^e\right) - s_{i,i-1}\left(\Pi_i^g - \Pi_{i-1}^e\right)\right], \quad (2.31)$$

where Π is the population and s is given, for low intensity, by

$$s_{m_g m_e} = \frac{\frac{\Gamma}{4}\frac{I}{I_0}\left\langle C_{m_g m_e}\right\rangle^2}{\Delta^2 + \frac{\Gamma^2}{4}} . \quad (2.32)$$

C is the Clebsch-Gordan coefficient for the transition. The steady state populations can be determined by solving the population rate equations [Walhout, *et al.* 1992]. The transitions involving maximum $|m_F|$ have the strongest coupling and, because of the selection rules for σ^+/σ^- light, pump the populations out of the $m = 0$ sublevel and into the maximum $|m_F|$ sublevels. The individual forces are also shifted away from the equilibrium value as seen in Fig. 2.5.

In the absence of a magnetic field these shifts are symmetric and yield an average force of zero at a velocity of zero, as expected. When a magnetic field is introduced the forces shift asymmetrically: the Zeeman shifts in the positive $|m>$ states increase the frequency separation (for $\vec{B}$ along the +z axis) while the negative $|m>$ states see a decrease in their separation as seen in Fig. 2.6.

At the velocity where both possible transitions from a particular ground state have the same frequency, the negative $|m>$ states are closer to resonance than the positive $|m>$ states (see Fig. 2.7) and, with a symmetric population distribution, would feel a stronger force. Population pumping compensates for this effect, shifting atoms from the negative $|m>$ sublevels to the positive ones. The average force on the atoms is zero for the condition

$$\vec{k} \cdot \vec{v} = -ge\mu_B B. \qquad (2.33)$$

This method of imparting a drift velocity to the atoms also has the possibility of raising the temperature of the atoms as it tends to disrupt the polarization gradient cooling [Lett, *et al.*, 1989, Walhout,

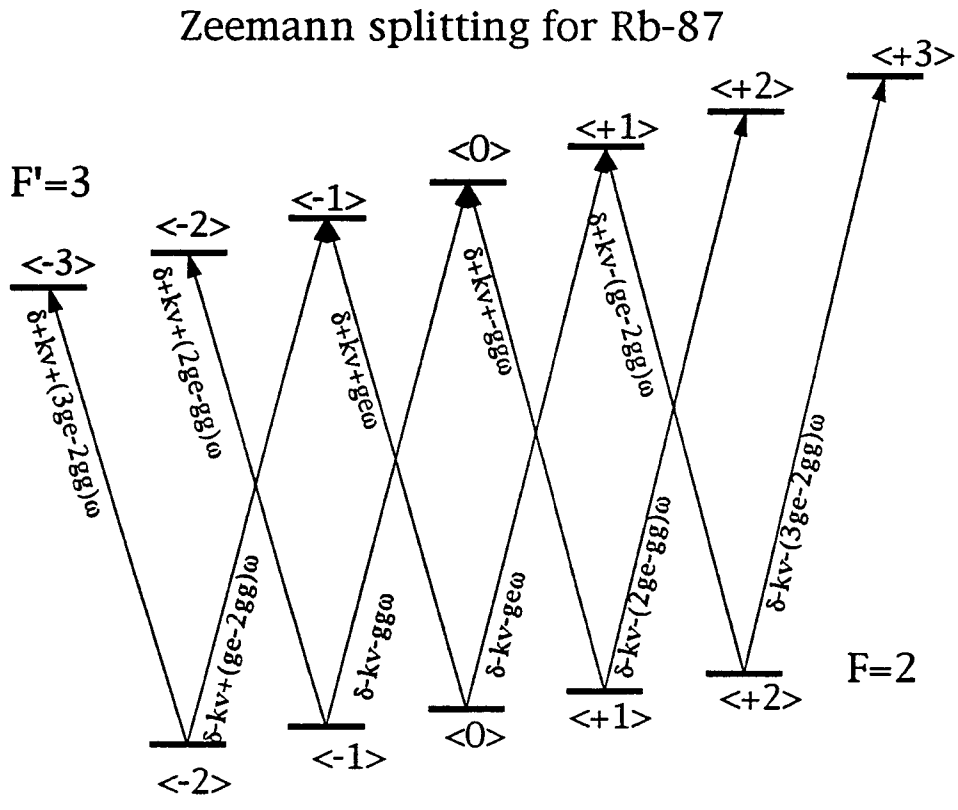

Fig. 2.6. Level splitting for ^{87}Rb showing Zeeman and Doppler shifts.

et al., 1992] because of the shifts in the ground state magnetic sublevels.

Rubidium

Alkali elements are often used for laser cooling and trapping experiments due to their relatively simple electron structure; they can easily be made to approximate a two level system. The D_2

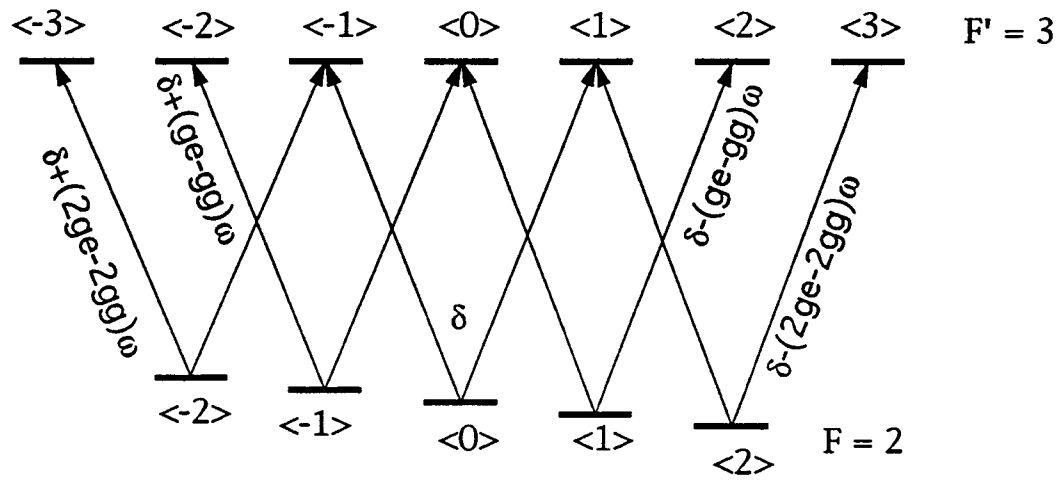

Fig. 2.7. Transitions for the condition $kv = -g_e\mu_B B$. Transitions from each ground state sublevel have the same frequency but an overall shift in the ground state still exists. Forces are balanced due to population shifts towards the |+m> states.

spectral line, whose transition connects the $^2S_{1/2}$ - $^2P_{3/2}$ states, can cycle with a closed hyperfine transition with $|\Delta m_F| = 1$ with circularly polarized light. The transition wavelengths are in the visible or near infrared: 589 nm for Na, 671 nm for Li, 766 nm for K, 780 nm for Rb and 852 nm for Cs. The Rb wavelength is accessible with inexpensive laser diodes and the relatively large mass of Rb reduces its rms velocity when cooled to the Doppler limit, so that the deBroglie wavelength spread $\Delta\lambda/\lambda$ will be small in the cold atomic beam.

There are two naturally occurring isotopes of rubidium, ^{85}Rb with nuclear spin I = 5/2 and ^{87}Rb with I = 3/2. ^{85}Rb is more abundant (72%) and is used in this experiment. The D_2 transition,

from the $5S_{1/2}$ ground state to $5P_{3/2}$ excited state, has a vacuum wavelength of 780.24 nm (780.03 in air) with a radiative lifetime τ of 26.5 ns. The hyperfine structure is shown in Fig. 2.3. The D_1 transition to the $5P_{1/2}$ state, sometimes used for optical pumping purposes, has its transition at 794.98 nm (794.76 in air).

The F = 3 to F′ = 4 hyperfine transition is used in the funnel and has a saturation intensity of 1.6 mW/cm^2. The Landé g-factors, used in calculating the Zeeman splittings, are $g_g = 1/3$ and $g_e = 1/2$ for the ground and excited states, respectively.

Chapter 3
Laser Operation

Diode Lasers

Diode lasers are relatively inexpensive sources of low power tunable laser light. We use commercially available AlGaAs diode lasers, Sharp model numbers LTO24 and LTO25 and Hitachi model number 7851G. These have a nominal wavelength ranging from 780 nm to 790 nm and output power of 20 - 50 mW. They are double heterostructure devices; the active region ($Al_yGa_{1-y}As$) is surrounded by p and n doped regions ($Al_xGa_{1-x}As$, x>y). A bias current injects electrons and holes into the active region, creating a population inversion, where recombination causes the emission of photons whose energy is equal to the bandgap of the material. A higher fraction of aluminum in the cladding makes the index of refraction of the active region higher than the cladding thus making the active region a waveguide. The ends of the laser are cleaved to act as mirrors; the large change in index (~3.5 -->1) gives ~30% reflection.

Diode laser wavelength and power output are dependent upon both injection current and temperature. Current flow changes the energy gap between the lowest empty level in the valence band and the highest filled level of the conduction band. Changes in temperature will affect the electron distribution in the two bands. The output wavelength will vary: ~0.3 nm/K for changes in

temperature and ~0.01 nm/mA for changes in current. (Values are for the Sharp laser diodes. Hitachi laser diodes have somewhat different characteristics) This behavior necessitates good temperature stability and a low-noise source of current in order to have frequency stabilized lasers. It allows tuning the laser to the desired frequency and also frequency modulation by direct manipulation of the injection current. Power output is also dependent upon injection current, varying at ~0.8 mW/mA above the lasing threshold so any frequency modulation of a laser diode results in amplitude modulation as well.

The small size of the active region causes diffraction at the facets and the rectangular cross section of the active stripe results in an elliptical beam in the far field. The angles of divergence are typically 30° for the major axis and 10° for the minor with polarization of the beam along the minor axis. Another feature of a diode laser is astigmatism: the rays of the major and minor axes originate from different points, so collimation of the beam in both transverse directions cannot be done with simple optics. If the beam cannot be accommodated within the collimating lens there will be diffraction in the beam but this and other spatial variations in the beam can be removed by spatial filtering.

Our laser diodes lase in a single longitudinal mode; a free running laser will lase in the mode which has the highest gain. Spacing of these modes is determined by the free spectral range (FSR) given by c/2nL, where n is the index (~3.5) of the laser material and L is its length. The Sharp lasers have a FSR of ~150 GHz which corresponds to 0.3 nm at the laser wavelength of

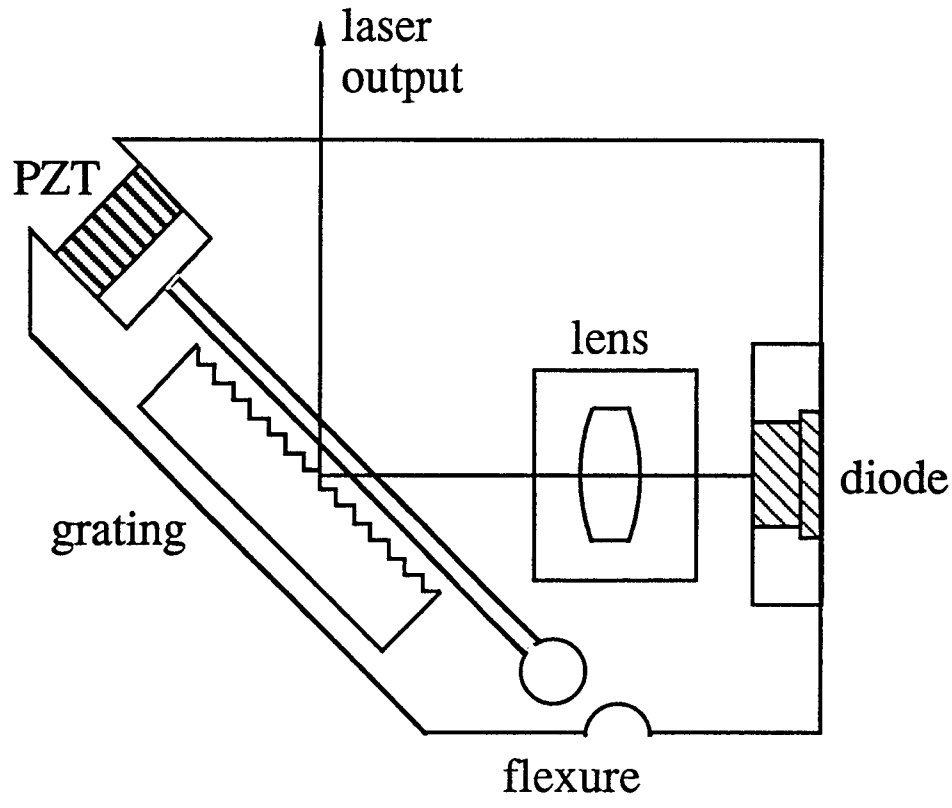

Fig. 3.1 Diagram of a diode laser module with optical feedback from a diffraction grating. The piezoelectric transducer (PZT) controls the grating's orientation and thus the wavelength of the light used as feedback into the laser.

780 nm. The gain curve, and thus the lasing mode, will vary with both temperature and injection current. The laser is also susceptible to sources of optical feedback which can be exploited to control the wavelength of the lasers.

Feedback Stabilized Diode Laser System

Linewidth narrowing and frequency selection are achieved via optical feedback from a diffraction grating [Maki, *et al.*, 1993]. The schematic of this layout is shown in Fig. 3.1. Additional electronic stabilization of the laser frequency is achieved by locking the laser wavelength to a Rb transition or optical cavity resonance via feedback from an integrating servo-control loop.

A holographic diffraction grating is mounted in the Littrow configuration to create an extended-cavity or coupled-cavity laser. (The diode laser itself is not modified and will oscillate by itself so this is not a true external-cavity laser). Most of the diffraction gratings were 1800 lines/mm which, at 780 nm, reflect 75% in the zeroth order, used as the laser output, and diffract 10% into the first order, used as feedback into the laser.

To achieve good thermal and mechanical stability the laser diode, collimating lens and diffraction grating were all mounted on a single piece of aluminum. The injection current is supplied by a battery driven low-noise current control circuit [Hemmerich, *et al.*, 1990]. The system is cooled below room temperature (~10 °C) and stabilized to several mK with a peltier element [Bradley, *et al.*, 1990]. Each laser module is housed within a Plexiglas enclosure to minimize thermal drifts caused by the laboratory's air conditioning unit.

To be used in this experiment, the proper combination of temperature and injection current must be found to yield the proper wavelength for the ^{85}Rb D_2 transition at 780.24 nm and

sufficient power to be able to saturate the transition with an approximately 1" diameter beam. Not all wavelengths are accessible at a given temperature, as the longitudinal mode spacing of the bare laser cavity is ±0.3 nm. Gaps in the tuning range are accessible by adjustment of laser current and temperature.

The grating is mounted on a small commercially available mirror mount which allows manual alignment of the extended cavity and adjustment of the feedback into the laser. Fine adjustment of the grating angle can be controlled electronically with a piezoelectric stack placed within the flexure shown in Fig. 3.1. Application of ±15 V provides extension of about ±1 μm, which provides precision tuning. This rotates and translates the grating to attempt to provide continuous tuning of a single longitudinal mode of the extended cavity [McNicholl and Metcalf, 1985]. The continuous tuning range of the extended cavity laser is 5-10 GHz before the laser hops to another extended cavity mode.

The mechanical vibrations of this system will limit the linewidth of the laser. Vibrations can be reduced by controlling the cavity length with feedback to the piezo stack but this is limited to frequencies below the mechanical resonance of the flexure. Since much of the mechanical noise will be at the resonance frequency the solution was to control the laser frequency with the laser injection current. The extended-cavity laser has a tuning of 250-500 MHz/mA (as compared to a free running laser tuning of 3 GHz/mA). The tuning range is limited to about 300 MHz before mode-hopping, but the mechanical noise in the system is well below this limit.

Etalon Locking: The Cooling Laser

For the chirped cooling laser, which requires continuous tuning over ~1.5 GHz (the entire Doppler profile of the ^{85}Rb absorption lines), the laser is stabilized to one side of the Airy transmission curve of a confocal Fabry-Perot etalon. A small fraction of the output beam (~4%) is directed into a 5 cm long etalon with a finesse of approximately 80. An integrating servo-control loop provides feedback to the laser current while the piezo element and etalon are synchronously scanned through the cooling chirp. The feedback corrects small deviations from synchronism as well as thermal drifts of the laser cavity. The system is robust enough to allow addition of a square wave (with a filter at 1 MHz) to the etalon driving signal to shift the cooling laser quickly off resonance.

Polarization Spectroscopy Locking: The Master Laser

To fulfill the requirement of having three separately tunable trapping lasers, we use a master-slave laser system. The master laser needs to be locked to a frequency near the F = 3 to F′ = 4 hyperfine transition. The master laser is locked to a polarization spectroscopy signal which provides a dispersive signal without modulating the laser frequency. Counterpropagating pump and probe lasers are used, with the pump beam nearly circularly polarized and the probe beam linearly polarized. The probe beam passes through the rubidium cell and then through a linear polarizer

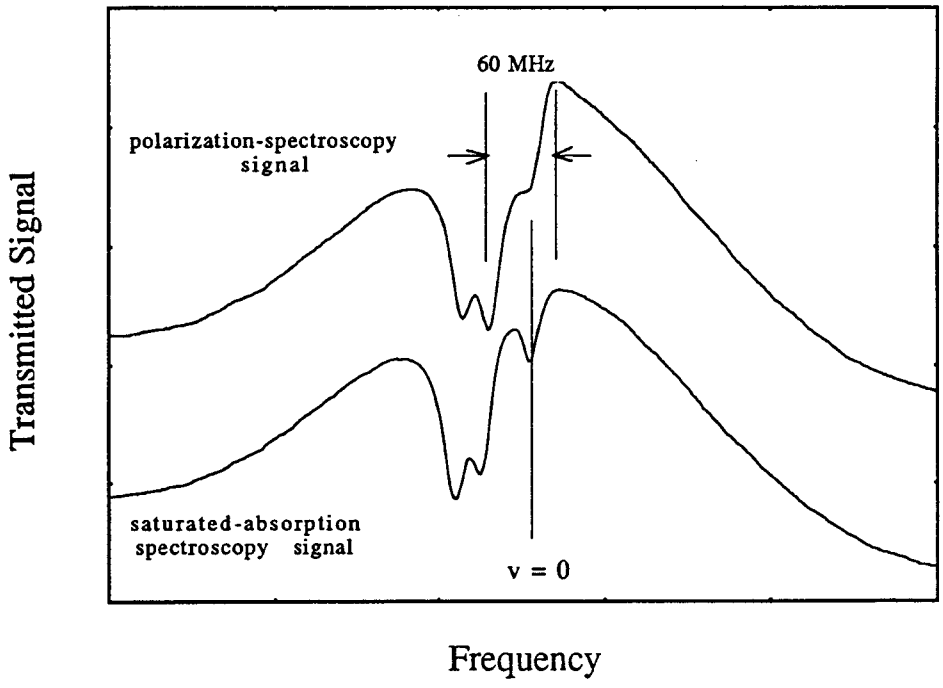

Fig 3.2. Spectra of the F = 3 ground state to the F′ = 2,3,4 excited state of the D_2 line of ^{85}Rb from a room temperature vapor cell. The lower trace is a standard saturated absorption spectrum. "v=0" designates the F=3 to F′=4 transition; also seen are two crossover resonances. The upper trace is the polarization-spectroscopy signal. The mostly linear region, used for servo-locking, is 60 MHz wide.

before being detected. Varying the amount of circular polarization in the pump beam and the orientation of the linear polarizer will yield many shapes in the output signal.

Fig. 3.2 shows the spectrum of the F = 3 to F′ = 2, 3, 4 hyperfine transitions of the D_2 line in ^{85}Rb. The available range for

locking is approximately 60 MHz, with usable linear regions on both sides of the $v = 0$ resonance. The trapping repump laser is locked, in a similar fashion, to the $F = 2$ to $F' = 3$ hyperfine transition.

Frequency Offset Locking: The Trap Lasers

The three trapping ("slave") lasers, designated **F**(ront), **B**(ack) and **V**(ertical), are each frequency-offset locked to the master laser to allow independent tuning with a minimum of frequency jitter. A small fraction (~4%) of the output beam of each of the trap lasers is heterodyned with a similar intensity beam from the master laser on a fast photodiode (flat frequency response up to 100 MHz). The resultant heterodyne signal is amplified by 30 dB and then sent to an electronic frequency discriminator. The output is then sent to an integrating servo-control loop whose feedback controls the slave laser's frequency offset from the master laser. Since the master has already been stabilized to a polarization spectroscopy signal, this locking mechanism passes the stability along to the slave lasers. The slave lasers' stability is of order 20-50 kHz from the fixed offset of 4-30 MHz from the master laser.

Before the final configuration was reached several combinations of frequency-offset locking and polarization locking were investigated. The difficulty that arises when more than one laser is locked with a polarization spectroscopy signal is that independent drift is present between the lasers. Each laser is dependent upon feedback from the polarization spectroscopy signal

which adjusts the injection current to that laser. Changes in the injection current also change the output power of the laser which causes a slight change in the polarization signal strength. The result is a small change in the DC level of the servo-control loop and thus a change in the frequency to which the laser is to be stabilized.

Using the frequency offset locking to directly link two of the trapping lasers introduced problems as well. The first drawback was the inability to produce a zero-velocity (static) trap since the laser frequencies could not be made degenerate. There was also optical feedback between the two horizontal lasers (F and B) which introduced electronic noise via the locking circuit. This noise was greatly diminished when the two lasers were not locked to each other.

Chapter 4
Laser Layout

Up to ten laser modules are used to perform the various tasks of laser cooling, optical molasses, trapping and probing. Each of these functions requires a laser tuned to the desired transition as well as a repump laser to offset the effects of optical pumping.

Each laser system has its own rubidium vapor cell and photodiode detector for monitoring the absorption signal of the laser (in the case of the trapping master laser and trap repump laser, these are polarization spectroscopy signals). When a laser is first turned on, or if it has drifted away from the vicinity of the absorption frequency, this signal is the indication that the laser is tuned to the proper frequency neighborhood. The laser schematic of the master laser and trapping lasers is shown in Fig. 4.1. The other lasers use similar schemes except the frequency offset locking.

Beam Expansion and Spatial Filtering

Each laser has its own beam expander to increase the major axis of the beam to 1". Beam expansion is achieved using two plano-convex lenses separated by the sum of their focal lengths, with the smaller focal length lens placed first to form a telescope. The three trapping lasers, for which wavefront quality is a concern, are spatially filtered. At the focus of the first lens of the beam

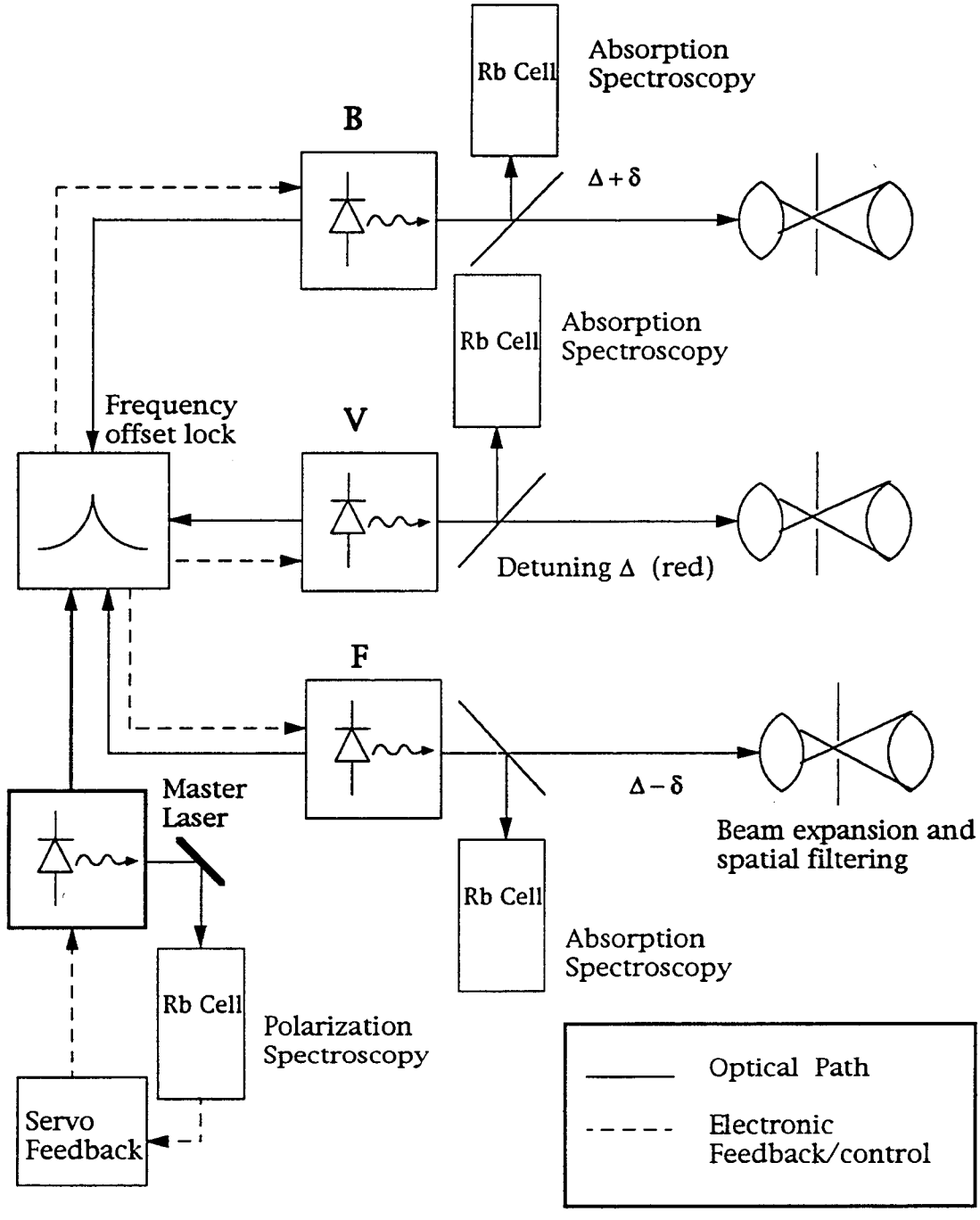

Fig. 4.1 Laser schematic. The three trapping lasers are heterodyned to a master laser to provide independent frequency offsets.

expander the spatial variation of the laser beam is a Fourier transform of intensity variations in the incident beam. A pinhole placed at this point will filter out any high-frequency spatial variation and allow only the lowest order Gaussian wavefront through. In practice, because of the diode laser's elliptical beam and susceptibility to optical feedback, this pinhole size is limited to no smaller than 30 μm in diameter. This effectively filters out variations along the major axis of the beam but is less effective for the minor axis. Using a smaller pinhole causes too much feedback and disrupts the laser to the point where it is not effective.

Spatial filtering will not remove low frequency spatial variations in the beam intensity. Each trapping beam is passed through a beamsplitter and these beams are recombined in the trapping region. Depending on the number of mirrors used to redirect each beam, the intensity profiles will either match or be opposed when they recombine. If a spatial variation in the intensity exists, and the recombined beam profiles are opposed, local intensity imbalances will result, causing corresponding variations in the scattering force.

Optical Isolation

The vertical trapping laser (V) and a retroreflected probe laser (discussed in a later section) each have a return path to the laser and are thus susceptible to feedback as from an extended cavity. For this reason an optical isolator is placed in the beam path.

In the case of the vertical trap laser, this is before the spatial filter. This greatly reduces, but does not completely eliminate, the problem of optical feedback. Fortunately only minor adjustments in the laser path will eliminate the problem and these alignment changes do not seem to affect the performance of the trap or probe laser.

Cooling Lasers

The beams from the cooling laser and its associated repump laser are combined with a beam splitter and passed through a pair of anamorphic prisms. These prisms have the function of expanding a beam in only one dimension, so the incident elliptical beam emerges as a nearly circular beam. This more closely matches the geometry of the hot atomic beam, so little of the laser beam is wasted on regions along the beam path which contain no atoms or atoms which have already acquired too large of a transverse velocity to survive to the trapping region. This arrangement also minimizes the amount of scattered light off of the copper collimation plate separating the oven chamber from the high vacuum chamber. Any scattered light serves to contaminate the video imaging of the trap and is a potential source of optical feedback into the cooling laser.

Trapping Lasers

To provide the circularly polarized beams necessary for trapping, $\lambda/4$ plates are placed are placed in each trapping beam's path just before it enters the high-vacuum chamber. In a three-dimensional MOT the $\lambda/4$ plates are oriented so that the trapping laser's angular momentum is in the direction opposed to the direction of $\vec{B}$.

In our two-dimensional case, with two laser pairs shifted 45° from the funnel axis, the three-dimensional $\lambda/4$ plate orientation is used to optimize trapping but trapping is still possible with significant deviations from circular polarization (~45° rotation of the $\lambda/4$ plate). This is due to the mixing of the transitions introduced by having the lasers at 45° to the Zeeman quantization axis. A very weak trap (very little fluorescence) has been observed with one $\lambda/4$ plate missing. Alignment of the vertical beam $\lambda/4$ plates is much more critical to observe trapping.

Fluorescence Detection

Fluorescence from atoms in the hot atomic beam, funnel and the cold atomic beam is detected using photomultiplier tubes (PMTs) and CCD cameras. One PMT, located at 45° above the trap, uses a 1" diameter, 100 mm focal length lens to image the trap region and detect any hot or cold atoms in the vicinity. One CCD camera also images this region from the direction that looks down

the atomic beam toward the oven. A second CCD camera can view the trap from the vertical direction if desired.

Probe Lasers

In order to detect the atoms which have been ejected from the funnel, two probe lasers, the gate-probe and molasses-probe, are used (see Fig. 4.2). The molasses-probe laser is aligned with optics located within the high vacuum chamber. A 1" mirror and $\lambda/4$ plate are mounted on a chassis inside the chamber and lined up with the end of the funnel wires. The linearly polarized incident light is retroreflected and forms a one-dimensional optical molasses region. The horizontal dimension was chosen for the molasses due to the geometry of the interferometer gratings: they are much taller than they are wide, so the molasses should retard expansion in the horizontal direction at the expense of some heating in the vertical direction. Fluorescence from this laser is imaged onto a photomultiplier tube using a 150 mm focal length lens mounted outside the vacuum chamber. This signal is used in time-of-flight measurements of the beam.

The gate-probe laser can be directed to any location from the end of the funnel to points several centimeters downstream. This laser is used to detect atoms at points outside the funnel during alignment of the lasers as the slow atomic beam may not be directed into the molasses-probe region. During time-of-flight measurements this laser is directed to the end of the trap region

and tuned to resonance to deflect the atoms away from the trap axis. An electronic square pulse is sent to the laser to move it off resonance for a short (3-5 ms) interval and allow the atoms to leave the trap and move along the trap axis where they can be detected by the fluorescence from the molasses-probe laser.

Each of these lasers has an associated repump beam which is split off from the trap repump laser. The gate-probe laser's repump is copropagating so that the combined laser beams may be easily moved along the atomic beam path. The repump for the molasses-probe is sent in along a separate path since the molasses-probe is retroreflected. To combine the repump laser with the molasses-probe laser would cause feedback on the repump laser.

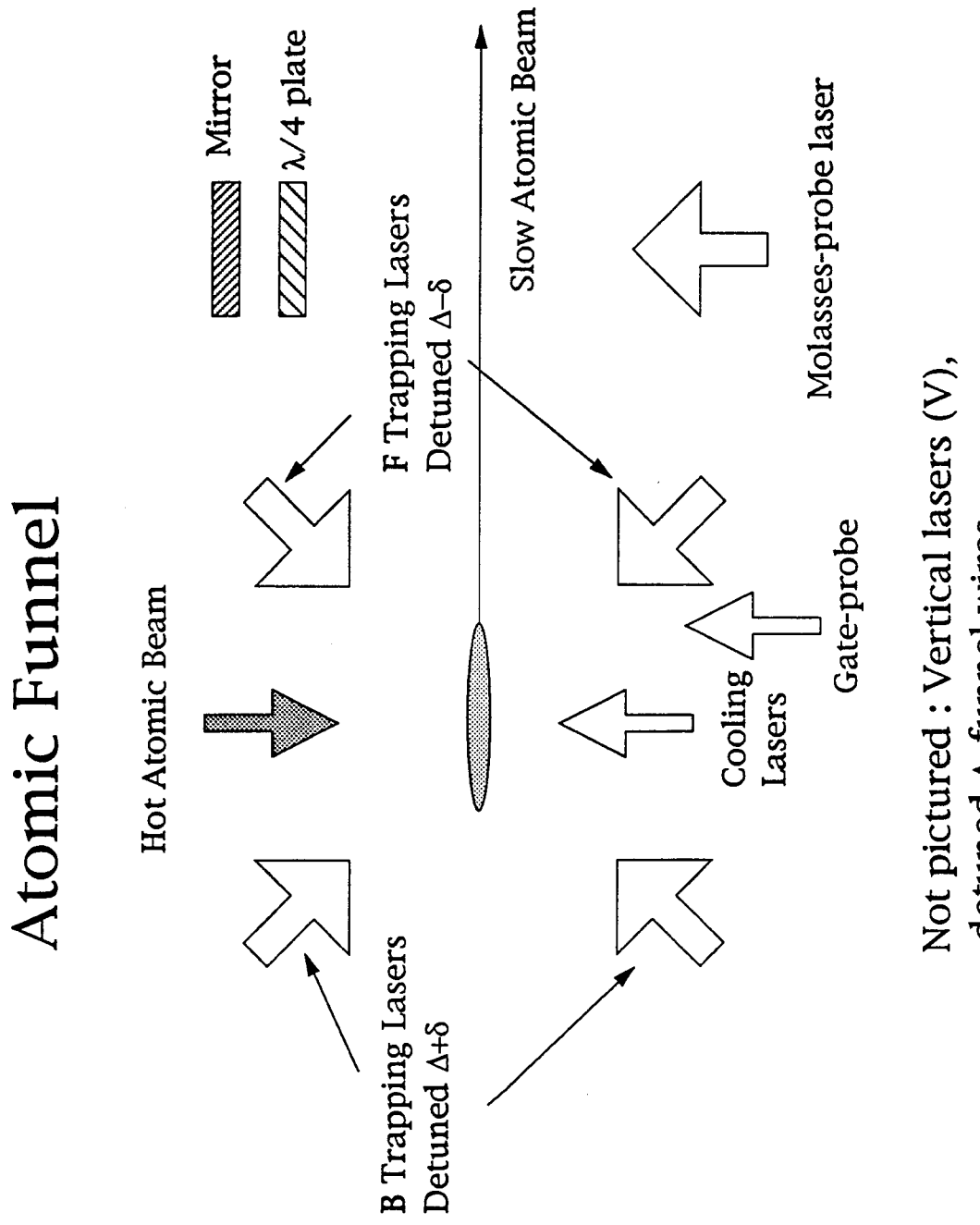

Fig. 4.2. Laser layout for the atomic funnel. View is from the top.

Chapter 5
Vacuum System

The rubidium source and funnel wires are housed in a differentially pumped dual chamber vacuum system. The oven chamber is pumped by a turbomolecular pump at a nominal pressure of ~1 x 10^{-7} torr and can be isolated from the turbo pump with the oven isolation gate valve. During standby or shutdown the pump is isolated from the high vacuum chamber by the chamber isolation valve. The high vacuum chamber is pumped by a diffusion pump, through a cryo-trap filled with methanol at -20 °C, to a pressure of ~1 x 10^{-8} torr. Isolation of the diffusion pump is possible with a pair of electropneumatic valves. A bypass arm allows roughing of the high vacuum chamber through a small liquid nitrogen trap without pumping through the diffusion pump. These components are shown in Fig. 5.1, the system schematic.

A nitrogen vent line is connected to the oven chamber, bypass arm, diffusion pump foreline and turbo pump venting port to allow each component to be vented separately. Nitrogen venting is especially desirable for both the oven and diffusion pump due to the presence of rubidium and (possibly hot) diffusion pump fluid, respectively, where the intrusion of oxygen and water could cause damage or reduce the efficiency of the components.

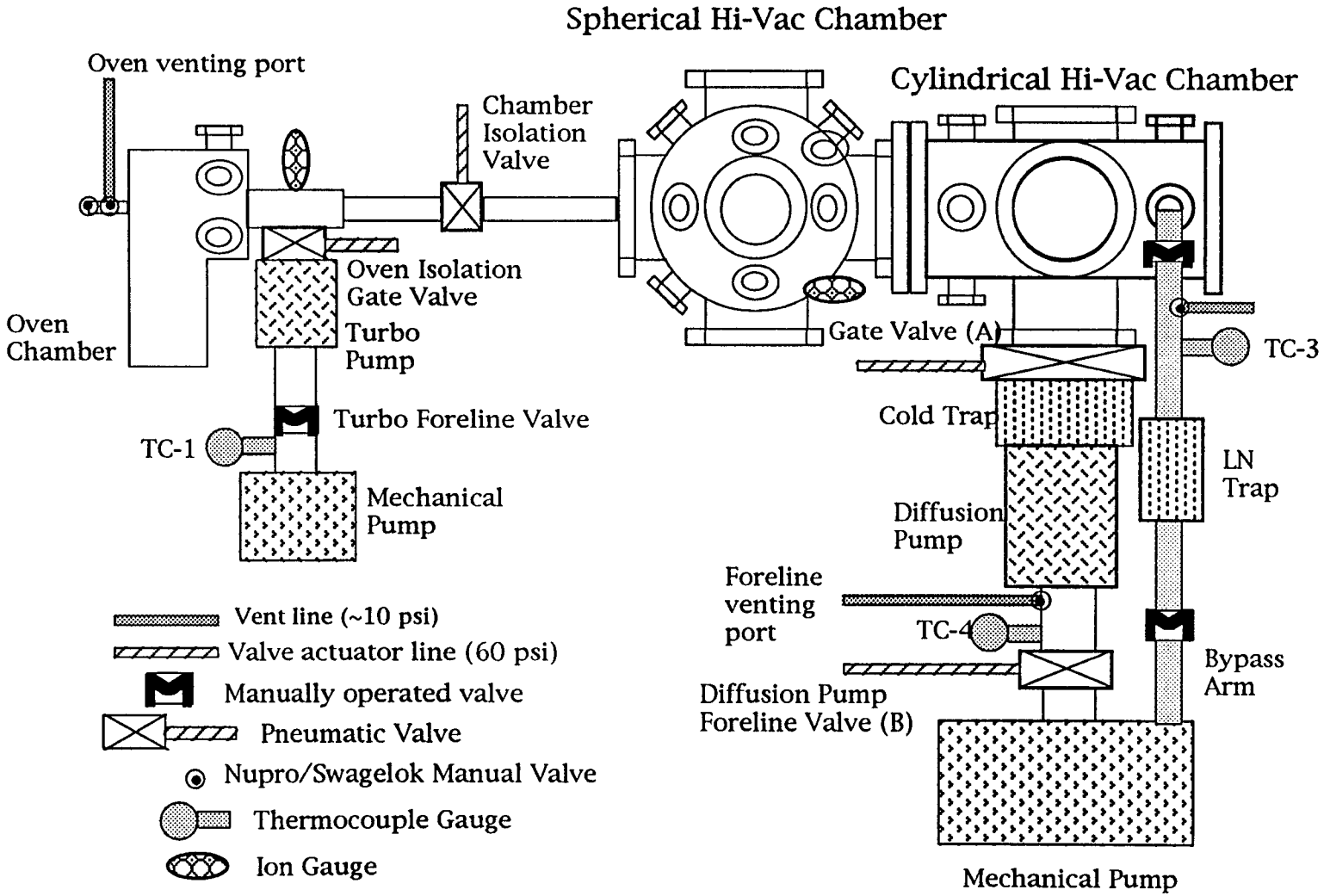

Fig 5.1. Vacuum system schematic.

Atomic Beam Oven

The oven, shown in Fig. 5.2, is constructed of stainless steel and is mounted in a housing with three kinematic support posts to allow leveling of the oven. This motion is largely restricted by the bellows connectors of the external condenser cup attached to the orifice flange. The housing anchors the oven with three screws at the vertical midpoint of the oven and a ball bearing at its base which reduces thermal losses to the rest of the apparatus. The oven has the capacity to house a 5 gram ampule of Rb which is loaded open end down to allow molten Rb to flow into the oven. This blocks the recirculation line of the recycling system so that the only escape of the Rb is through the 0.040" diameter orifice at the end of the nozzle. The copper condenser cup, kept at 12-15 °C with a water cooling line, catches the rubidium that is not directed near the beam axis and solidifies the metal on the condenser and in the recirculation line. Thermocouples on the oven body, nozzle, orifice flange and condenser cup allow the temperature of the various portions of the system to be monitored. The orifice flange also has a conical pocket drilled on the outside to reduce the length through which the atoms must travel to ~0.15". One version of the oven had a cylindrical pocket drilled on the oven side of the flange, reducing the orifice to ~0.050" in length, but this design was abandoned because the pocket tended to fill with rubidium and clog the orifice.

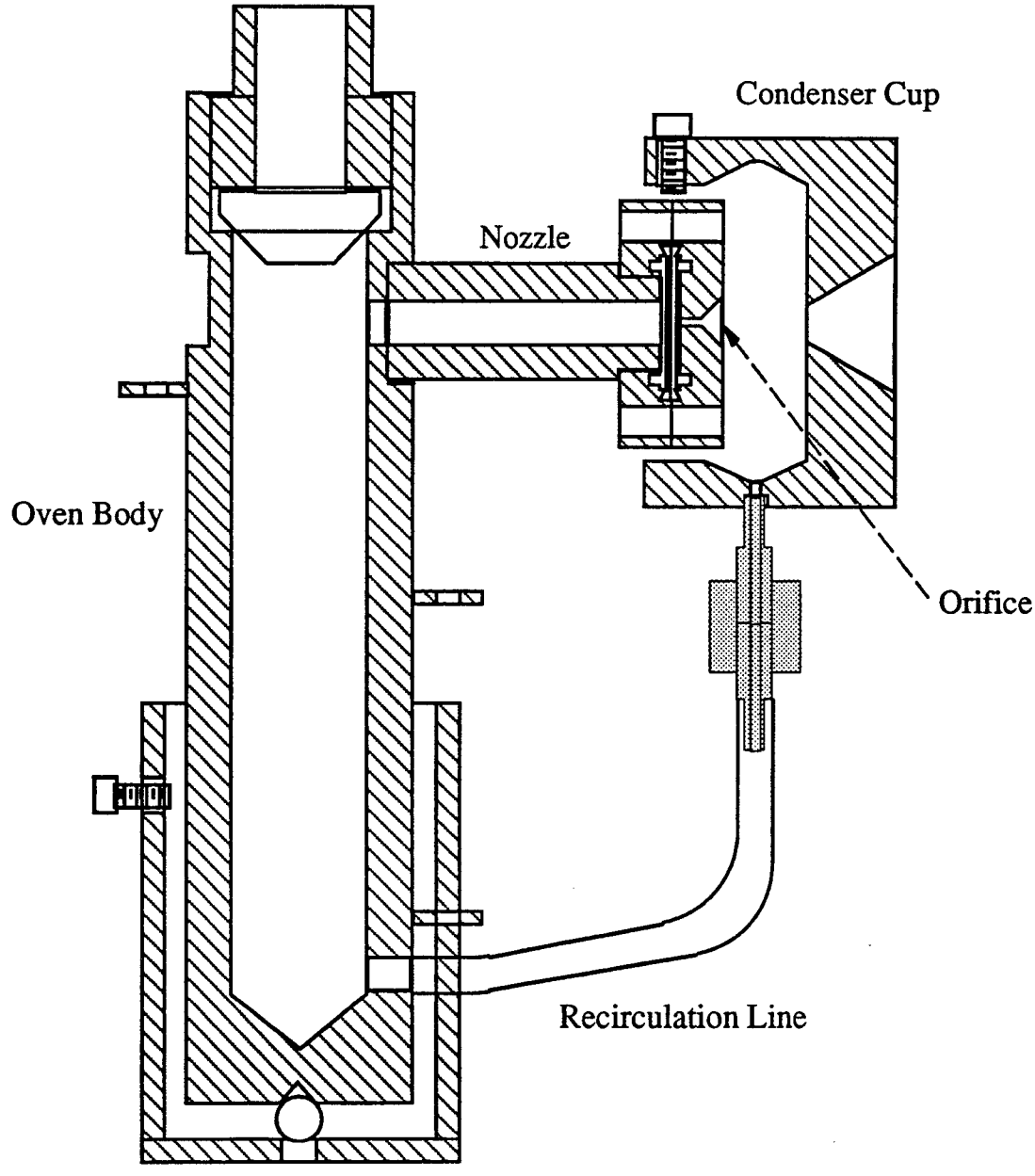

Fig. 5.2. The rubidium oven.

Resistive heating is used on three separate areas of the oven: the nozzle, oven body and recirculation line. During standby the nozzle heater is supplied with ~1.2 A to keep the system at ~60 - 80 °C (above the Rb melting point) to avoid clogging of the orifice. During operation the nozzle and orifice are kept hotter than the oven body to avoid condensation of liquid on the nozzle. The nozzle heater is supplied with 3.7 A - 4.4 A (AC) to heat the orifice flange to ~240 - 250 °C. (The current has changed over the life of the oven as the characteristics of the heater has changed. The quality of thermal contact can change slightly each time the oven is opened for maintenance, and the number of windings has also changed.) The oven body is maintained at ~235 °C with a current of ~1.5 A.

At these temperatures the oven can be operated for about six hours before the risk of overloading the recirculation system [Lambropoulos and Moody, 1977, Carter and Pritchard, 1978] requires that the oven be shutdown and the captured rubidium be recycled. If the amount of rubidium is too great the reservoir at the base of the condenser cup will become clogged and subsequent rubidium deposition will, in the course of one or two heating cycles, form a bridge between the orifice flange and the condenser cup. This causes the orifice flange and nozzle temperature to drop well below the oven temperature and a significant amount of rubidium will condense and block the orifice and nozzle. Manual removal of the metal is required to return the oven to operation.

The recycling procedure starts with the oven at standby. The condenser cup cooling water is turned off and the line is purged

with nitrogen and the nozzle current and recirculation line current are increased to ~2.5 A. The condenser cup is slowly allowed to heat to ~80 °C which causes the collected metal to liquefy and drain through the recirculation line into the oven. The metal in the recirculation line solidifies when cooling water is restored to the condenser cup. Recycling dramatically increases the lifetime of each ampule of rubidium and thus reduces the frequency of exposure of the oven to air while reloading. A 5 gram ampule of rubidium can last through 60 cycles of beam operation/recycling before replenishment is necessary. We estimate that ~1 gram of Rb may be present in the condenser cup after six hours of beam operation.

When oven maintenance is required the oven must be cooled to room temperature by letting the system sit overnight. Work on the heater wires or other components external to the oven can sometimes be done with roughly half of the system still housed in the vacuum chamber with the nitrogen vent line open. This will minimize the oxidation of rubidium that has collected on the outside of the oven. Work on the oven requires complete removal from the chamber.

The oven is cleaned, prior to loading a new ampule into the system, with ethanol and deionized water. It is then dried and reloaded into the chamber to be roughed out to ensure that all of the solvents have been adequately removed. Care must be taken to ensure that as little rubidium as possible is left in the oven prior to cleaning as reactions with water can be somewhat violent and ethanol will ignite. The condenser cup and nozzle flange are

removed and cleaned and the recirculation line is checked for blockage.

System Protection

Automatic shutdown and interlocks help protect the vacuum pumps and oven from damage due to loss of power or water and, in some cases, loss of vacuum integrity. Portions of the automatic system can be bypassed and operated manually as is normally done during startup and planned shutdowns.

Water flow switches close when adequate flow is present and act as an interlock to prevent starting a pump without cooling water. On loss of power or water to the system the power to the electropneumatic valves will be interrupted and the valves will close to isolate the pump from its associated vacuum chamber and also turn the pump off. Subsequent reintroduction of power and/or water will not reopen the valves without operator intervention so that the appropriate restart procedure may be used.

Each pump has a pair of foreline pressure setpoints (interlock and hysteresis) tied into the protection system. The interlock setpoint (the lower of the pair) must be reached before the pump can be started. If the pressure subsequently rises above the associated hysteresis setpoint then the protection circuitry will automatically be engaged and the valves will close. While this will not protect the pump against a catastrophic exposure to atmosphere it has protected the diffusion pump fluid against slow leaks on three

Fig. 5.3. The wires of the atomic funnel. View is perpendicular to the funnel axis, which runs left - right, and along the hot beam/cooling laser axis. The inner wires are separated by 1". Also seen are the support bars at bottom, lens holder for fluorescence detection at upper left and laser alignment target on feedthrough at upper right.

separate occasions; once against a crack in the ceramic seal of a feedthrough and twice against leaks in the solder joints of the atomic funnel water cooling system before the funnel was replaced by a single tube design.

The Atomic Funnel

The magnetic field for the atomic funnel is provided by a large current passing through copper tubing arranged to approximate the

quadrupole field of four parallel infinite straight wires at the vertices of a square (see Fig. 5.3). The original configuration used 1/8" O.D. tubing soldered into a continuous conductor and attached to a dual tube water cooled electrical feed-through. The inner wires were separated by 0.75", the spacing of the feed-through tubing. The solder joints failed on two occasions when water cooling was lost while current was still present, so the funnel was changed to a single tube design, with the corners bent rather than soldered. The tubing was changed to 3/16" O.D. Two mirror image tubes were used and the feed-through changed to a four tube design, separated at 1.0", with a return tube separation of 2.5". Supports mounted at the base of the high vacuum chamber attach to the return-path tubes to maintain proper orientation of the funnel. A target on a linear feedthrough can be inserted into the trap region for laser alignment.

Chapter 6
Beam Operation

Funnel Operation

In preparation for operating the funnel, the current to the nozzle heater is changed from its standby value to its operating value and, after about one hour, the oven heater is turned on. This maintains the nozzle at a higher temperature to minimize the risk of clogging. System heatup takes about 2 hours, during which time the lasers can be turned on, adjusted and tuned to the rubidium transition. At the oven operating temperature of ~235 °C the rubidium vapor pressure in the oven is of order 0.1 torr with an output density of ~5 x 10^{10} cm^{-3} in the atomic beam, measured by absorption of a low intensity resonant laser, at ~1 cm outside the condenser cup.

When the system is at operating temperatures the chamber isolation valve is opened to connect the two parts of the vacuum system. A "wobble stick" allows the atomic beam to be blocked before entering the high vacuum chamber; this is moved out of the way during normal operation. The gasket next to the chamber isolation valve is a solid copper disk with a 0.30" diameter hole that acts as a collimator for the atomic beam. Geometric expansion of the beam from the orifice through the collimator and transverse heating yield a beam ~2 cm in diameter in the funnel region. The cooling lasers are focused to try and match the atomic beam profile and

minimize the losses due to beam expansion. At the entrance to the high vacuum chamber (near the trap) the cooling laser has a diameter of ~2 cm and an intensity of 5 mW/cm^2.

Slowing Atoms in the Hot Beam

The cooling and repump lasers are scanned or "chirped" to cool the atomic beam. The chirp rates are adjusted to maximize the PMT signal from atoms brought to zero velocity. The scan is started ~450 MHz away from the zero velocity resonance, which corresponds to an atom velocity of 350 m/s. The scan uses a sinusoidal chirp rather than a linear (sawtooth) chirp to avoid the presence of any high frequency harmonics that might correspond to mechanical resonances with the piezo stack or the flexure arm that holds the grating. When the chirp is near the zero velocity resonance an electronic square pulse with a filter at 1 MHz is added to the sinusoidal chirp to move the cooling laser quickly away from this resonance. This stops the slowing and cooling at a velocity, determined by the placement of the square pulse, known as the "cutoff velocity." This also prevents the cooling laser from strongly interacting with the atoms in the trap.

The frequency at which the cooling laser is cut off with the square pulse must be chosen carefully: chirped cooling brings the atoms to their final velocity at the same time, as opposed to Zeeman slowing, which brings atoms to their final velocity at the same position, so the atoms at the cutoff velocity may be located several

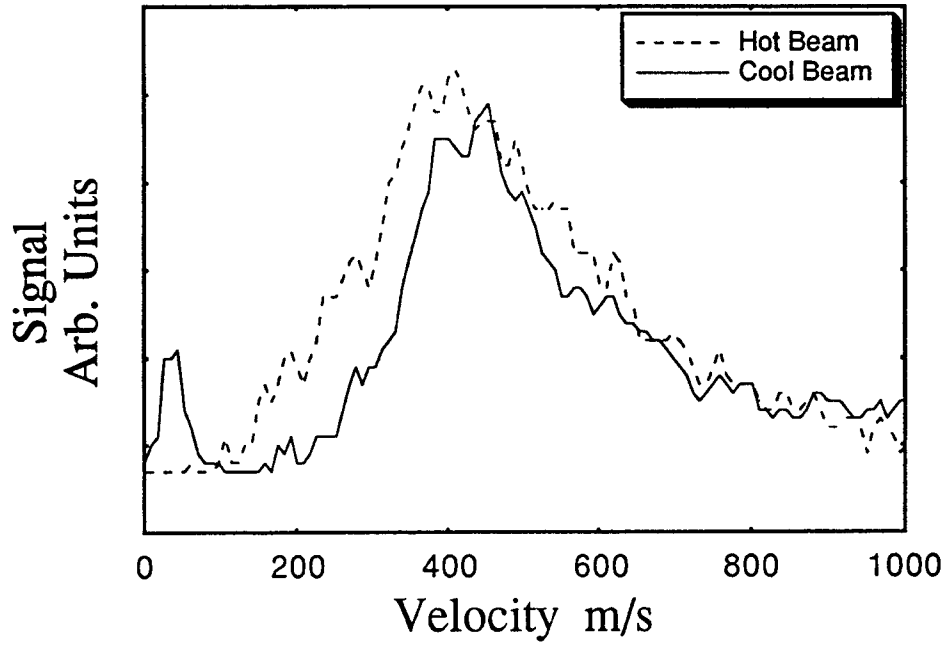

Fig. 6.1. Fluorescence signal from a hot atomic beam and a laser cooled atomic beam. The laser chirp begins at ~350 m/s and slows the atoms to ~25 m/s.

centimeters from the trap region. Due to the transverse heating which must accompany the longitudinal cooling, these atoms not near the trap region when the final velocity is achieved will tend to diverge and miss the trap. A higher cutoff velocity reduces the divergence angle and allows for more efficient loading. To give the best loading the cutoff occurs when the atoms have been slowed to a maximum velocity of ~20-25 m/s. This range is in excellent agreement with the capture velocity predicted by equation (2.27) which, assuming a 1.0 cm capture radius, gives a value of 24 m/s.

A computer model using a numerical integration of the trap forces from equation (2.12) also agrees, yielding a value of 20 m/s as the capture velocity for a trap laser detuning of -2Γ.

A comparison of the hot and cooled beams is shown in Fig. 6.1. A probe laser, at 45° to the atomic beam and passing through the center of the high vacuum chamber, was scanned over the velocity profile and the fluorescence was recorded for both a hot beam and for a beam that had been slowed by chirped cooling. The cooled beam shows a marked decrease in signal for velocities below the start of the cooling chirp and a large signal at the cutoff velocity.

Trapping Beam Alignment

To facilitate easy alignment of the trapping beams a target was mounted on a 2" linear motion feed-through with access to the center of the funnel trapping region. The target is a wafer of stainless steel in which a hole has been drilled. The target is oriented along the <111> plane of the coordinate system defined by the trap lasers, which allows ~2 mm of clear aperture through which each laser may pass. An iris diaphragm centered in each beam path reduces the beam size to ~2 mm for this alignment. To ensure that the beams are also level, a stiff paper target is placed over each window and the laser is aligned to the center of the window and then allowed to pass through the target. The lasers are iteratively adjusted until they are level and pass through the center of the funnel region. This alignment is good enough to immediately form a

trap which can subsequently be improved by fine-tuning the laser alignment.

Trapping

In order to trap atoms in the funnel the current to the funnel wires is turned on and set to 70 A (DC), generating a radial magnetic field gradient of ~12 G/cm in the trapping region. This field is shown in Fig. 6.2. Though this field gradient is smaller near the end of the funnel it is sufficient to confine the atoms and the beam diameter does not noticeably increase. A small axial component is present from the connections between the inner wires and their return path.

The master laser is then locked to a frequency a few MHz to the blue of the F = 3 to F′ = 4 resonance. Locking onto the resonance itself is not possible since the polarization spectroscopy signal is much flatter there than on either side. Locking on the red side would not allow proper locking of the trap lasers since the frequency offset lock is limited to a minimum of ~4 MHz and is sensitive to minor acoustic vibration (as from talking) up to ~8 MHz and the back laser may need to be within a linewidth of resonance when frequency offsets are introduced. The trap lasers are typically adjusted to an offset of 15 MHz with respect to the master laser, which gives an overall detuning of two linewidths. The trapping repump laser is then placed on the F = 2 to F′ = 3 transition so that the atoms will be trapped and fluoresce, at which

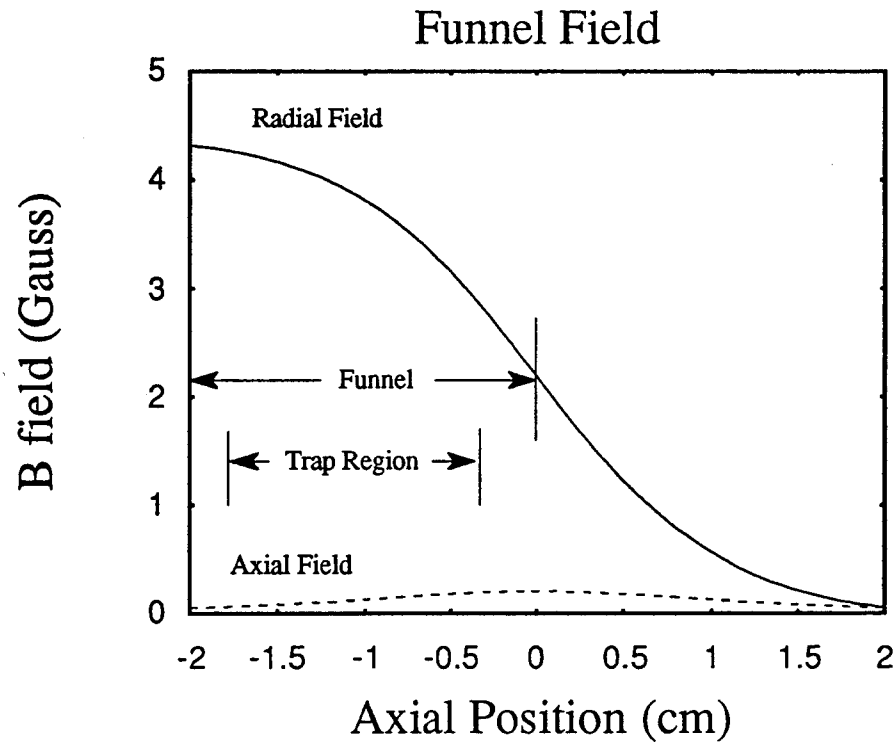

Fig. 6.2. The funnel magnetic fields. Solid line is the radial (trapping) field and the dotted line is the axial field from the connections between the inner and outer wires, for a current of 70 A and location of 3 mm off axis. On axis all fields are zero. The trap region extends from approximately -1.75 to -0.25 cm.

time this laser is locked. This produces a "static" trap: with all three trap lasers at the same frequency the atoms will feel no net scattering force only when they are at rest. The front and back trap lasers can then be offset with respect to each other to eject the atoms along the axis of the funnel.

Since the locking range of the trap lasers is effectively ~8 - 30 MHz and both the front and back lasers are locked to the same

side of the master laser, the frequency offsets, $\delta = (\omega_{back}-\omega_{front})/2$, are limited to ~9 - 10 MHz, allowing for ejection velocities of ~10 m/s. Larger frequency offsets can be achieved by locking the master laser to the red side of the $v = 0$ resonance and inverting the locking signal on the front laser to lock to the blue side of the master laser. Frequency offsets attainable in this fashion are ~10 MHz to ~20 MHz, so beam velocities in excess of 20 m/s are accessible with this system.

The trap lasers have intensities well above saturation, with ~9 mW/cm^2 in the vertical laser and ~7.5 mW/cm^2 in the front and back lasers.

The cold atomic beam emitted from the funnel is pulsed due to the chirped cooling method of loading. The trap itself operates continuously. A continuous loading system, such as Zeeman slowing, will yield a continuous cold beam from the funnel.

Chapter 7
Data Acquisition and Analysis

For the beam of atoms generated by the atomic funnel to be useful as a source for an atomic interferometer, a controllable beam velocity of order 10 m/s must be achievable. In addition, the beam temperature must be as low as possible to minimize the transverse spreading, which affects the usable flux of atoms, and to minimize the wavelength spread $\Delta\lambda/\lambda$, which dictates the coherence length of the atomic beam. Data were taken to measure the cooled beam characteristics of intensity, longitudinal and transverse temperature (where temperature is a measure of the velocity spread induced by the interaction with the lasers), and variation of velocity with frequency offset and magnetic field. The beam characteristics are compared to the values predicted by the theory presented in chapter 2.

Transverse Temperature

The transverse temperature was estimated from CCD camera images of the trap and molasses-probe region. Upon leaving the funnel the cold atomic beam should expand in proportion to its transverse velocity. It was assumed that the flight from the trap to the molasses-probe region occurred with no laser interaction and thus no acceleration. The spatial extent of the fluorescence from the

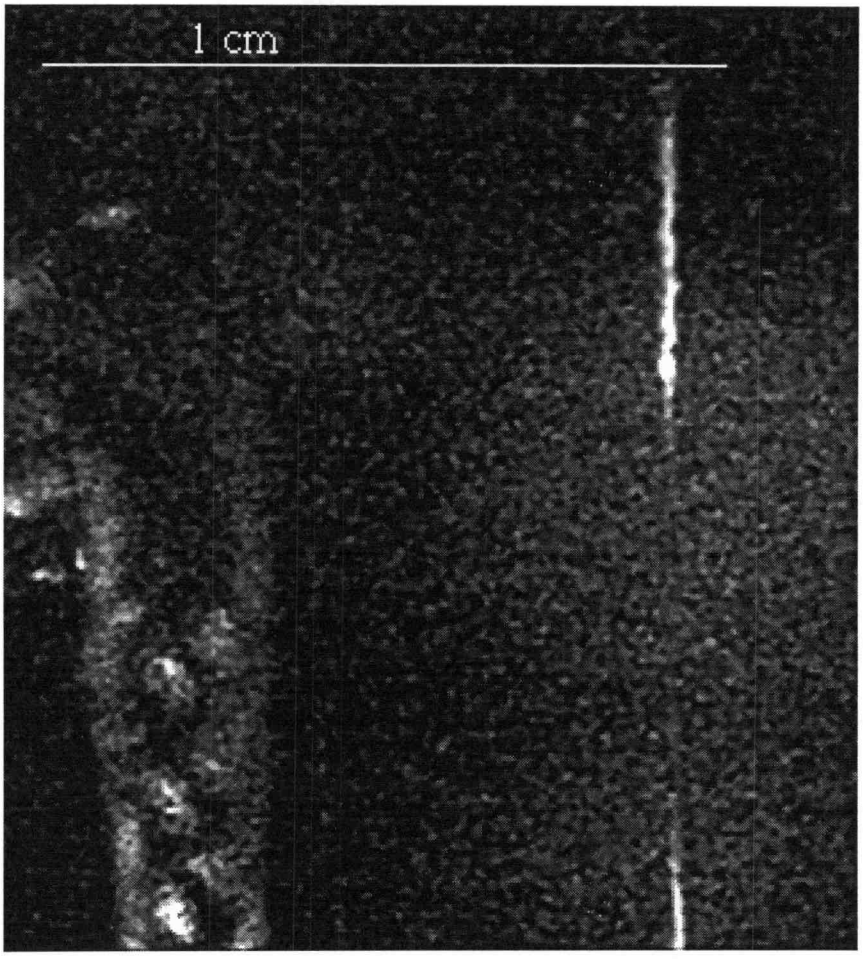

Fig. 7.1. Top view of atomic funnel. Fluorescence at bottom is from trapped atoms. Fluorescence at top is from atoms in the molasses-probe.

molasses-probe laser was recorded and measured, and from this the transverse velocity and temperature were determined. The transverse velocity in one dimension is given [Joffe, *et al.*, 1993] by:

$$v_{\perp} = \frac{\sqrt{d_f^2 - d_i^2}}{2t} \tag{7.1}$$

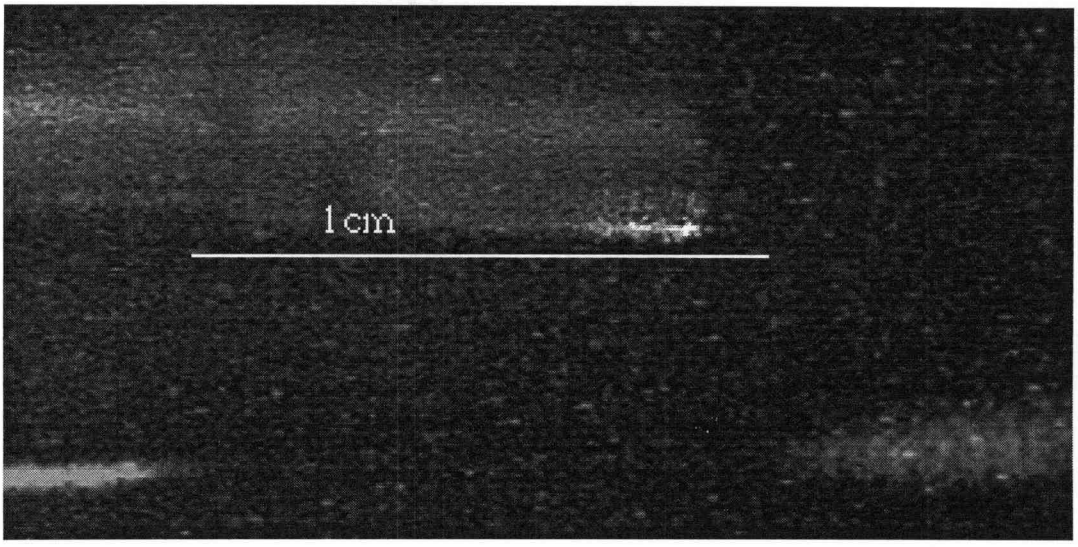

Fig. 7.2. Side view of atomic funnel. Atoms on left are in the trap region and ejected to the right. Fluorescence from ejected atoms is due to the molasses-probe laser.

where d is the final/initial beam diameter and t is the travel time from funnel to detection. With the typical detuning of -2Γ in the molasses, the Doppler cooling limit, from equation (2.22), is 310 μK.

From two measurements taken from the vertical view, shown in Fig. 7.1, the horizontal transverse temperature was determined to be $120\ ^{+60}_{-40}$ μK, using $Mv^2/2 = k_BT/2$. This temperature is below the Doppler cooling limit. This is in the direction of the retroreflected molasses-probe and within 2 cm of the end of the funnel where the presence of magnetic fields (refer to Fig. 6.2) makes some confinement possible. Extensive quantitative corroboration of this value has proven difficult to achieve due to excessive scattered light into the vertical camera.

The vertical transverse temperature was measured eight separate times. In this dimension transverse heating from the molasses-probe is present and the effects are quite apparent on resonance, so the molasses-probe is detuned ~Γ to avoid a pronounced divergence of the beam. Measurements of the beam diameter were made at the end closest to the funnel so that this heating could be ignored. Temperatures as low as $380^{+80}/_{-70}$ μK were measured and were generally not higher that 600 μK. The trap can be seen from this view in Fig. 7.2.

Funnel Population

A photomultiplier tube was calibrated to allow a fluorescence measurement of atoms in the funnel. A signal of 40 mV was recorded at a calibration of 1.5 nW/mV. A lens to improve light gathering subtended 0.016 of the total solid angle and was assumed to image one-half (7.5 mm) of the trapping region. The ejection velocity was 5 m/s for the duration of the ~6 msec unloading, so only ~1/4 of the atoms contribute to the instantaneous PMT signal. If one assumes the atoms scatter photons at the maximum rate (one photon per 2τ) and that the lasers are on resonance this signal is equivalent to ~2×10^7 atoms. A detuning of 2Γ combined with power broadening change the scattering rate by a factor of ~20, so a single chirp results in ~4×10^8 atoms leaving the funnel. With a chirp rate of 25 sec^{-1} this gives 10^{10} atom/s leaving the funnel

region. With a trap diameter of 0.5 mm and a length of 15 mm this is a density of 3.4 x 10^9 atom/cm^3.

Beam Intensity

The number of atoms in the funnel should be equal to the number of atoms detected after the atoms have been ejected. A measurement of the fluorescence from the molasses-probe region was made, using a different PMT than in the previous section. A 1.15 nW signal was detected, representing 8.7 x 10^5 atoms, under the assumption of maximum scattering rate and resonance. The pulse, traveling at 4 m/s, was recorded in a detection region of ~1 mm. With a total pulse width of ~6 msec, the signal represents 1/24 of the total pulse. Detuning of order Γ and power broadening reduce the scattering rate by a factor at least eight, so the signal represents a total pulse population of ~1.6 x 10^8 atoms, or a total intensity of 4 x 10^9 atoms/s. This is in general agreement with the population measured inside of the funnel.

Velocity

Time-of-flight measurements were made to determine the velocity and longitudinal temperature of the atoms. Fluorescence from the molasses-probe laser was detected with a PMT. The molasses-probe laser had an intensity of 22 mW/cm^2 and was

1 mm wide by 3 mm tall. The gate-probe laser, ~2 mm in radius with an intensity of 27 mW/cm^2, was used to deflect the cold beam away from the molasses-probe detection region. A pulse of atoms was then allowed to travel from the funnel to the detection region. The gate was opened for 3 - 5 ms and then closed to define a square pulse that would evolve in shape due to the beam's longitudinal temperature. The atoms traveled distances of 15 - 20 mm from gate to the detection region for these measurements, though fluorescence has been detected an additional 20 mm further from the funnel and an as-yet uncalibrated hot-wire signal 30 cm from the funnel is present. A comparison of an unmodified pulse and a gated pulse is shown in Fig. 7.3.

The atoms in the funnel are not confined along the funnel axis. They should behave as a one-dimensional Boltzmann gas, whose velocity distribution is given by

$$N(v) = \frac{N_{tot}}{\alpha\sqrt{\pi}} e^{-(v-v_{drift})^2/\alpha^2} dv \ , \tag{7.2}$$

where

$$\alpha = \sqrt{\frac{2k_B T}{M}} \ . \tag{7.3}$$

The quantity α is the characteristic width of the velocity profile. The distribution function can be rewritten in terms of time t and the distance of travel d from funnel to detection to represent a point source of atoms:

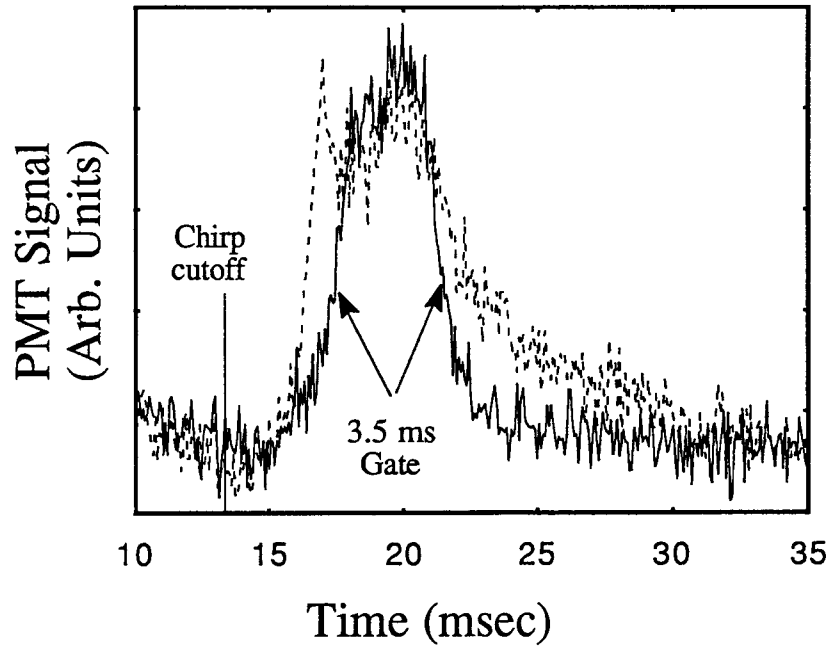

Fig. 7.3. Molasses-probe signal. The outer, dotted line is the unmodified unloading pulse from the funnel. The inner, solid line is an unloading square pulse created with a 3.5 msec gate.

$$N(t) = \frac{N_{tot} d}{\alpha \sqrt{\pi t^2}} e^{-\frac{\left(\frac{d}{t} - v_{drift}\right)^2}{\alpha^2}} dt \,. \tag{7.4}$$

The equation for α is modified [Riis, *et al.*, 1990] to account for the width, σ_p, of the molasses-probe laser:

$$\alpha = \sqrt{\frac{2k_B T}{M} + \frac{\sigma_p^2}{t^2}} \,. \tag{7.5}$$

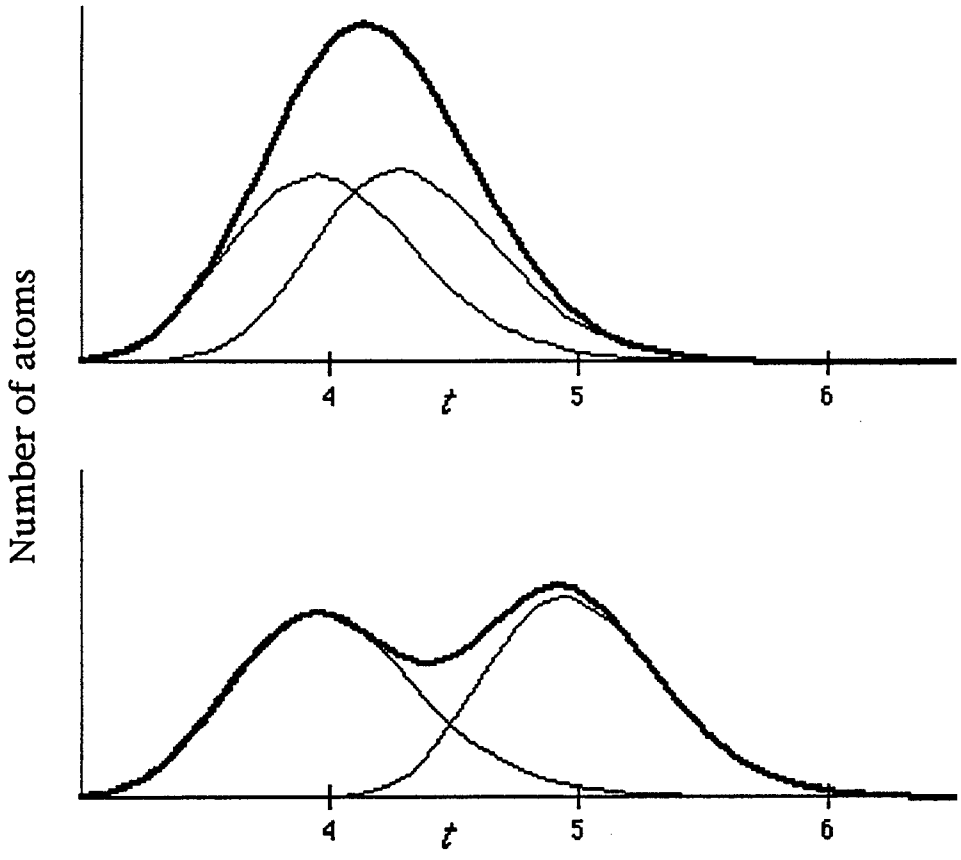

Fig. 7.4. Graphs showing the beam model. Velocity is 3 m/s at a distance of 12 mm and T = 500 μK. Top graph shows two point sources separated by 1 mm. Bottom graph shows two point sources separated by 3 mm. Dark line is the sum of the point sources.

The performance of a linear source of length L is modeled by adding together point sources separated by a distance δL. For these point sources to model a continuous trap the separation δL must be small compared to the physical spreading of a point source due to its temperature as it evolves in time, so $\delta L < \alpha t$ or $\delta L < \alpha d/v$. To gain reliable temperature data to a resolution of 500 μK with

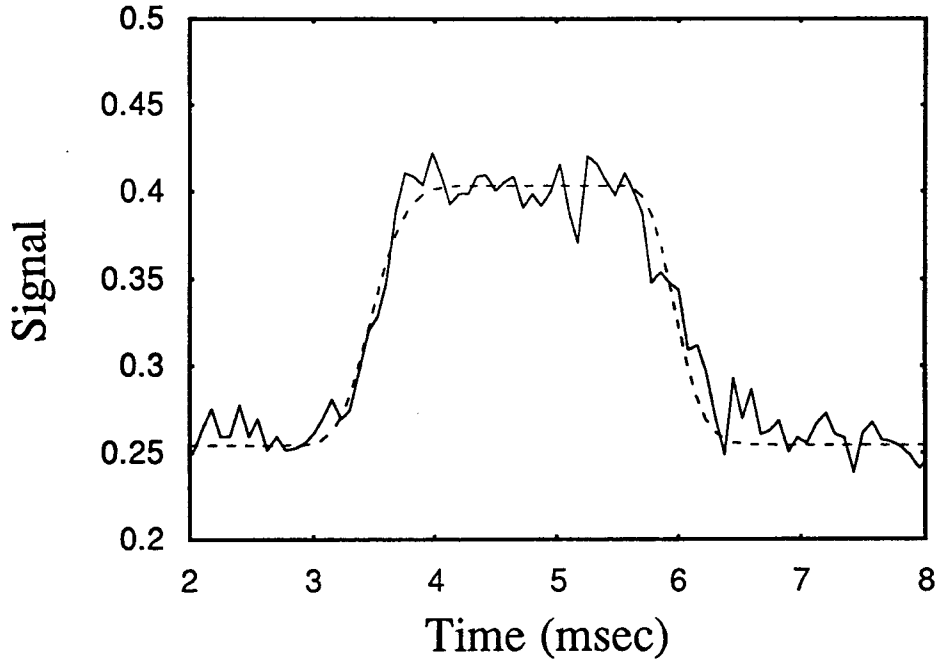

Fig. 7.5. Data and theory using equation (7.4). The data represents a PMT signal from the molasses-probe fluorescence with a laser detuning of 2.6 MHz and a distance of 17.2 mm from gate to molasses. The theoretical curve (dashed line) represents a velocity of 4.8 m/s at a temperature of 500 μK.

$\delta L = 1$ mm and $d = 12$ mm, the atom velocity must be below ~4 m/s, as shown in Fig. 7.4. Larger velocities and colder temperatures can be modeled using smaller increments.

The linear source of atoms is subjected to the resonant gate-probe, which produces a square pulse of atoms leaving the trap. At the detection region the signal will no longer be square: the atoms are at some temperature, so a group of atoms leaving the gate at the same time will not arrive in the detection region at the same time.

This causes a decrease in slope of the leading and trailing edge of the PMT signal from the fluorescence induced by the molasses-probe.

In this model the length of the trap, L, is not the physical length of the trapping region, which is ~1 cm. The funnel loads over a period of ~6 msec and the funnel behaves as if the source were of length $L = v_{eject} t_{load}$ with each point source emerging from the trap and traveling the distance d to the detection region. If the gate is of short enough duration then the pulse of atoms can be assumed to be of reasonably uniform strength, so the gate was kept as short as possible.

The measurements using the gate were compared to the model based on equation (7.4) and a sample data set is shown in Fig 7.5. The trap length L was iteratively calculated using $L = v_{drift} t_{gate}$. The free parameters in the model are amplitude, velocity and temperature. The detection time interval, dt in equation (7.4), is incorporated in the amplitude.

The velocity and temperature are independently determined parameters for a given distance d. The velocity is determined by d and the time interval from gate opening/closing to the corresponding increase/decrease in the PMT signal. Fig. 7.4 indicates that for a sufficiently large value of L the atoms at the leading edge of a pulse, at the opening of the gate, will behave independently of the trailing edge.

The longitudinal temperature is determined primarily by the slope of the edges of the convoluted square pulse. This analysis yielded results consistent with a beam with longitudinal

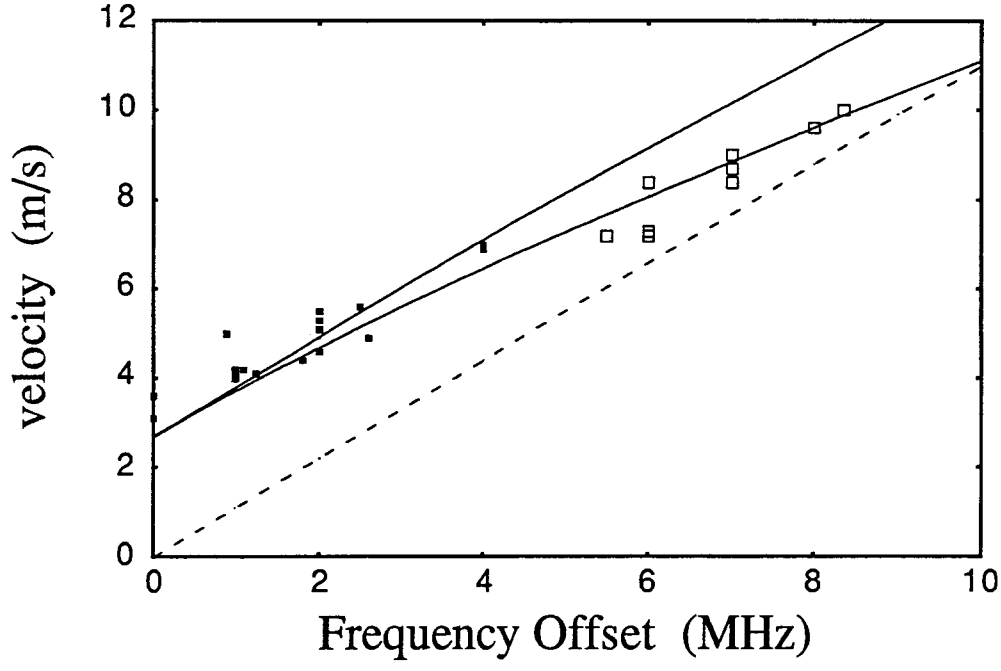

Fig. 7.6. Velocity dependence on frequency offset. The squares represent the time-of-flight data. Filled points indicate a nominal detuning of -2Γ (low velocity) and unfilled points indicate a nominal detuning of -3Γ (high velocity). The solid lines represent the predictions of the model with a 3.5 G axial bias field with nominal detuning of -2Γ (upper) and -3Γ (lower). The dashed line represents the terminal velocities expected with no bias field.

temperatures as low as $500\ ^{+500}_{-250}$ μK. This overlaps with the cooling limit of 310 μK expected for a detuning of -2Γ and is consistent with the vertical transverse temperature.

Time-of-flight data were taken with frequency offsets ranging from zero to 8.35 MHz. The velocity variation with laser frequency offset, δ, should vary as equation (2.29), whose slope is 1.1 $^{m/s}/_{MHz}$.

As can be seen from Fig. 7.6, there is significant deviation from this prediction, especially at low velocities. The presence of fluorescence from the molasses-probe at zero laser offset indicates the presence of a bias in the net detuning or intensity imbalance in the trapping/molasses lasers. The laser intensities are above saturation and the intensity differences are very small, so the overall contribution to an offset velocity is negligible.

A detuning bias may be introduced with an axial magnetic field. From CCD images of the trap region it was determined that the trap is displaced 2 - 3 mm from the axis, so an axial field is present (shown in Fig. 6.2) but is smaller than 0.2 G. A small contribution to an axial field may be due to a combination of the earth's magnetic field and asymmetries in the funnel wires, but these contributions are also of order 0.2 G. A large contribution could be due to the six magnetic bases attached to the vacuum chamber frame, used to hold mirrors and the light collecting lens for one of the PMTs. To quantify these effects a single magnetic base was placed next to the chamber and the time-of-flight was measured for opposite orientations of $\vec{B}$. This produced a ±0.7 m/s shift in velocity at a frequency offset of $\delta = 1$ MHz. This is the velocity shift produced by a ~1 G field, according to equation (2.33), $\vec{k}\cdot\vec{v} = -g_e\mu_B B$. A series of measurements taken with fields produced by Helmholtz coils external to the chamber confirm this relationship.

A larger field will, of course, produce a larger velocity shift. The results from a model using the numerical integration of the forces in a 3.5 G axial field over a trap length of 10 mm is included with the velocity data in Fig. 7.6. In this model the atoms were

assumed to have no axial velocity as they entered the funnel and are accelerated due to forces produced by the laser frequency offsets and the axial magnetic field.

The low velocity atoms ($\delta \leq 4$ MHz) show a larger shift in velocity than the high velocity atoms. At low velocity the nominal detuning is $\Delta = -2\Gamma$ and the transit time is several times longer than the damping time τ_c given by equation (2.17), which is 470 μs. These slow atoms are accelerated to their terminal velocity well before leaving the trap. At higher frequency offsets, Δ is changed to -3Γ to keep the frequency of the B laser far enough away from the master laser to ensure that B remains locked. This reduces the scattering rate and increases the damping time to 1.3 ms. This is almost as large as the transit time through the trap and results in a significantly smaller velocity shift as the terminal velocity is not attained.

The position damping seems to occur on a time scale as short or shorter than the velocity damping, as observations show the diameter of fluorescence from the trap to be equal at both ends. If the spatial damping time were significantly longer than the velocity damping one would expect a "wedge" profile in the funnel as the atoms are slowly forced to the axis and ejected.

Conclusions and Future Research

The performance of this atomic funnel represents an improvement over the other reported funnels as a source of cold,

low velocity atoms and its completion is a significant step toward the goal of constructing an atomic interferometer. The target velocity of 10 m/s has been achieved and the system has the capability of reaching higher velocities if this becomes necessary. The beam density and flux are consistent with other reported values [Riis, *et al.*, 1990, Nellessen, *et al.*, 1990 and Yu, *et al.*, 1994] but with the necessary advantages of a clear path on the funnel axis and simultaneous molasses cooling along the axial and transverse dimensions. The resulting temperatures are close to the limiting values for Doppler cooling to allow for minimal transverse expansion and longitudinal wavelength spread.

The planned move of the apparatus to its permanent location will allow for the removal of the magnetic bases now being used. The removal of the external magnetic field may allow for low temperatures due to orientational cooling. The introduction of Zeeman slowing will significantly improve the flux of atoms to be used as the interferometer source.

Bibliography

Anderson, A., S. Haroche, E. A. Hinds, W. Jhe, D. Meschede and L. Moi, Phys. Rev. A **34**, 3513 (1986).

Balykin, V. I., V. S. Letokhov, Yu. B. Ovchinnikov and A. I. Sidorov, JETP Lett. **45**, 353 (1987); Phys. Rev. Lett. **60**, 2137 (1988).

Bauspiess, W., U. Bonse, H. Rauch and W. Treimer, Z. Physik **271**, 177 (1974).

Berkhout, J. J., O. J. Luiten, I. D. Setija, T. W. Hijmans, T. Mizusaki and J. T. M. Walraven, Phys. Rev. Lett. **63**, 1689 (1989).

Bjorkholm, J. E., R. R. Freeman, A. Ashkin and D. B. Pearson, Phys. Rev. Lett. **41**, 1361 (1978).

Bonse, U. and M. Hart, Appl. Phys. Lett. **6**, 155 (1965).

Bradley, C. C., J. Chen and R. G. Hulet, Rev. Sci. Instrumen. **61**, 2097 (1990).

Carnal, O. and J. Mlynek, Phys. Rev. Lett. **66**, 2689 (1991).

Carnal, O., M. Sigel, T. Sleator, H. Takuma and J. Mlynek, Phys. Rev. Lett. **67**, 3231 (1991).

Carter, G. M., and D. E. Pritchard, Rev. Sci. Instrum. **49**, 120 (1978)

Chu, S., L. Hollberg, J. Bjorkholm, A. Cable and A. Ashkin, Phys. Rev. Lett. **55**, 48 (1985).

Chu, S., D. S. Weiss, Y. Shevy and P. Ungar, *Atomic Physics 11*, S. Haroche, J. C. Gay, G. Grynberg, eds., World Scientific, Singapore (1989). p. 636.

Dalibard, J. and C. Cohen-Tannoudji, J. Opt. Soc. Am. B **6**, 2023 (1989).

Dalibard, J., C. Salomon, A. Aspect, E. Arimondo, R. Kaiser, N. Vansteenkiste and C. Cohen-Tannoudji, *Atomic Physics 11*, S. Haroche, J. C. Gay, G. Grynberg, eds., World Scientific, Singapore (1989). p. 199.

Delfs, H., *A Magneto-Optic Trap for Rubidium*, M.S. Thesis, Oregon State University (1992).

Estermann, I. and O. Stern, Z. Phys. **61**, 95 (1930).

Greenberger, D.M., Rev. Mod. Phys. **55**, 875 (1983).

Hänsch, T. W. and A. L. Schawlow Optics Commun. **13**, 68 (1975).

Hemmerich, A., D. H. McIntyre, D. Schropp Jr., D. Meschede and T. W. Hänsch, Optics Comm. **75**, 118 (1990).

Joffe, M. A., W. Ketterle, A. Martin and D. E. Pritchard, J. Opt. Soc. Am. B **10**, 2257 (1993).

Kasevich, M. and S. Chu, Phys. Rev. Lett. **67**, 181 (1991).

Keith, D. W., C. R. Ekstrom, Q. A. Turchette and D. E. Pritchard, Phys. Rev. Letters **66**, 2693 (1991a).

Keith, D. W., M. L. Schattenburg, H. I. Smith and D. E. Pritchard, Phys. Rev. Lett. **61**, 1580 (1988).

Keith, D. W., R. J. Soave and M. J. Rooks, J. Vac. Sci. Technology B **9**, 284 (1991b).

Lambropoulos, M. and S.E. Moody, Rev. Sci. Instrum. **48**, 131 (1977)

Lett, P. D., W. D. Phillips, S. L. Rolston, C. E. Tanner, R. N. Watts and C. I. Westbrook, J. Opt. Soc. Am. B **6**, 2084 (1989).

Lett, P. D., R. N. Watts, C. I. Westbrook, W. D. Phillips, P. L. Gould and H. J. Metcalf, Phys. Rev. Lett. **61**, 169 (1988).

Maki, J. J., N. S. Campbell, C. M. Grande, R. Knorpp and D. H. McIntyre, Optics Comm. **102**, 251 (1993).

Martin, P. J., B. G. Oldaker, A. H. Miklich and D. E. Pritchard, Phys. Rev. Lett. **60**, 515, (1988).

McNicholl and Metcalf, Appl. Optics **24**, 2757 (1985).

Monroe, C., W. Swann, H. Robinson and C. Wieman, Phys. Rev. Lett. **65**, 1571 (1990).

Nellessen, J., J. Werner and W. Ertmer, Optics Comm. **78**, 300 (1990).

Raab, E. L., M. Prentiss, A. Cable, S. Chu and D. E. Pritchard, Phys. Rev. Lett. **59**, 2631 (1987).

Riehle, F., Th. Kisters, A. Witte, J. Helmcke and Ch. J. Borde, Phys. Rev. Lett. **67**, 177 (1991).

Riis, E., D. S. Weiss, K. A. Moler and S. Chu, Phys. Rev. Lett. **64**, 1658 (1990).

Sheehy, B., S-Q Shang, R. Watts, S. Hatamian and H. Metcalf, J. Opt. Soc. Am. B **6**, 2165 (1989).

Steane, A. M., M. Chowdhury and C. J. Foot, J. Opt. Soc. Am. B **9**, 2142 (1992).

Walhout, M., J. Dalibard, S. L. Rolston and W. D. Phillips, J. Opt. Soc. Am. B **9**, 1997 (1992).

Werner, S. A., Phys. Today, Dec. 1980, p. 24.

Wineland, D., and H. Dehmelt, Bull. Am. Phys. Soc. **20**, 637 (1975).

Yu, J., J. Djemaa, P. Nosbaum and P. Pillet, Optics Comm. **112**, 136 (1994).

Appendices

Appendix A
Gratings for Atomic Interferometry

The gratings for the atomic interferometer were constructed at the National Nanofabrication Facility (NNF) at Cornell University over a two week period in the spring of 1992 with the assistance of Dr. Michael Rooks. The procedure was based upon one developed by Keith, *et al.* [1991b] for an interferometer using a supersonic Na beam [Keith, *et al.*, 1991a].

Fabrication of the gratings required forming a membrane of silicon nitride on a silicon substrate, writing the grating pattern in an electron beam resist and using a directional etch to remove the exposed pattern. The grating duty cycle must be large enough to give a detectable throughput and the wires strong enough to support themselves during processing and handling. In order to actually see interference they must be phase coherent over their entire area: the lines must be straighter than a line width over their entire length.

Local Fabrication

The gratings were to have been constructed with the aid of Dr. Martin Wybourne at the University of Oregon using a converted electron microscope as an electron beam writing device. After further investigation of the process it was decided that the grating

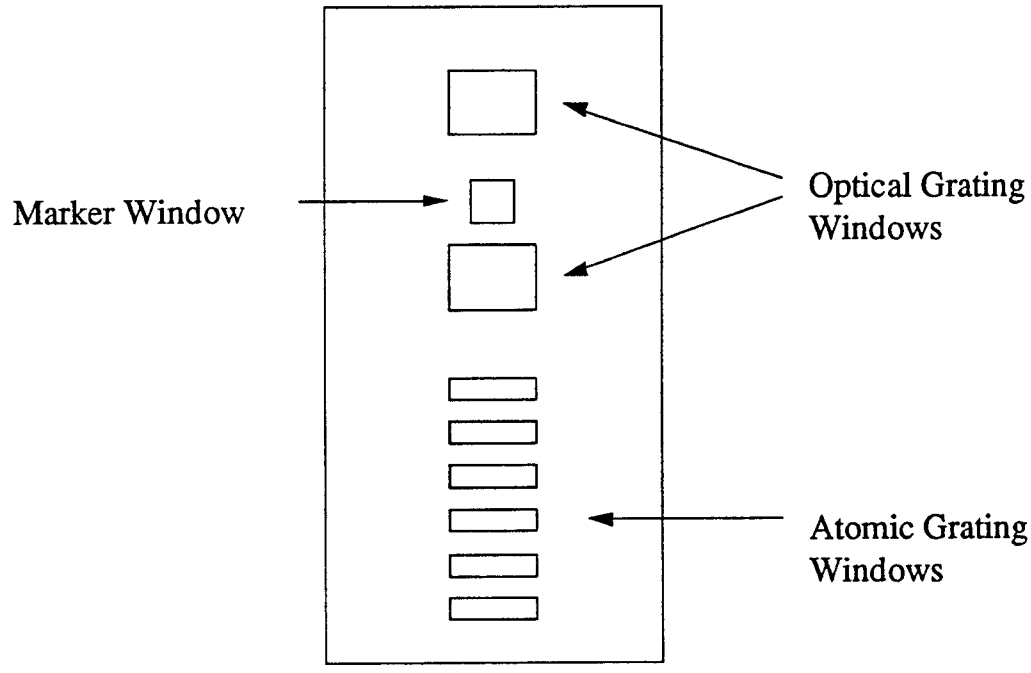

Fig. A.1. Photomask layout for each chip.

requirements were too stringent for local production. Silicon wafers were to be processed locally by depositing silicon nitride with plasma enhanced chemical vapor deposition. However, the silicon nitride had small defects that allowed etching of the silicon underneath and the byproduct gas (H_2) blew the nitride off of the wafer.

NNF Fabrication

Double polished 3" diameter silicon wafers were coated, on both sides, with ~120 nm of low stress silicon nitride using low

pressure chemical vapor deposition (LPCVD) prior to my arrival at NNF.

The membranes are produced by placing a window pattern on the back side of the silicon wafer with contact photolithography, removing the silicon nitride and then etching through the exposed silicon. A Chrome photomask was produced with a CAD program. Each mask contained patterns for 20 chips, each 12 mm x 7 mm, with six rectangular windows for atom gratings, two windows for optical gratings and one marker window as shown in Fig. A.1. Break lines were marked at the chip boundaries so that the chips could later be separated. The backside of the silicon wafer was coated with photoresist and exposed with the Chrome mask at 405 nm. Alignment of the mask with the crystal axis was achieved by cleaving the end of the wafer. The front of the wafer (which is the back side during this process) is protected by also coating with a resist. Two masks, with grating windows of width 50 μm and 150 μm, were produced. Seven chips on each mask had windows 0.5 mm in height and 13 had 1.0 mm windows. A third mask to make large scale (750 mm square) gratings was made but not used in this trip to NNF.

The nitride exposed by the photolithography is removed by a reactive ion etch (RIE) process and then the silicon is removed by immersion in a ~6.5 M KOH solution (660 g KOH in 1650 ml H_2O) at 93 °C. The KOH etches ~50 times faster in the <100> direction than it does in the <111> direction, so on a 250 μm thick wafer the windows will shrink by ~180 μm on each side (It was for this reason that break lines for each chip were made 80 μm wide: the KOH would

not etch all the way through the silicon and the chips would break apart at the proper places). A view of a KOH etched window is shown in Fig. A.2. The KOH etched through the wafers in ~150 minutes. Some small (~200 nm) silicon nodules were left after this etching process, but longer etches in KOH tended to destroy some of the membranes. Removal of these nodules was also attempted with an isotropic silicon etch (H_2O:HNO_3:HF, 75:150:1) but this caused some defects to appear in the nitride and was not used in later production.

The front side of the wafer was then spin coated with ~200 nm of polymethyl methacrylate (PMMA), an electron beam resist, and then with ~20 nm of gold via thermal evaporation (e-beam deposition emits x-rays and exposes the PMMA). The purpose of the gold is to minimize charging of the substrate during the electron beam exposure which can cause beam writing distortions. The e-beam writer, a JEOL JBX 5DII, produces a 50 keV beam that can be focused to a spot of ~20 nm. In the "U" mode used for writing these gratings the beam writes in an 80 μm x 80 μm field. To produce larger patterns successive fields must be coherently "stitched" together by moving the positioning stage which holds the chips. The positioning stage is monitored with a laser interferometer with an accuracy of better than 5 nm.

Errors in the grating pattern can be due to errors within each writing field and stitching errors. Errors in each writing field, due to distortions in the lens or beam steering system, tended to be small. Field stitch errors are caused by thermal drifts in the workpiece dimensions, thermal drifts in the beam column, gain and

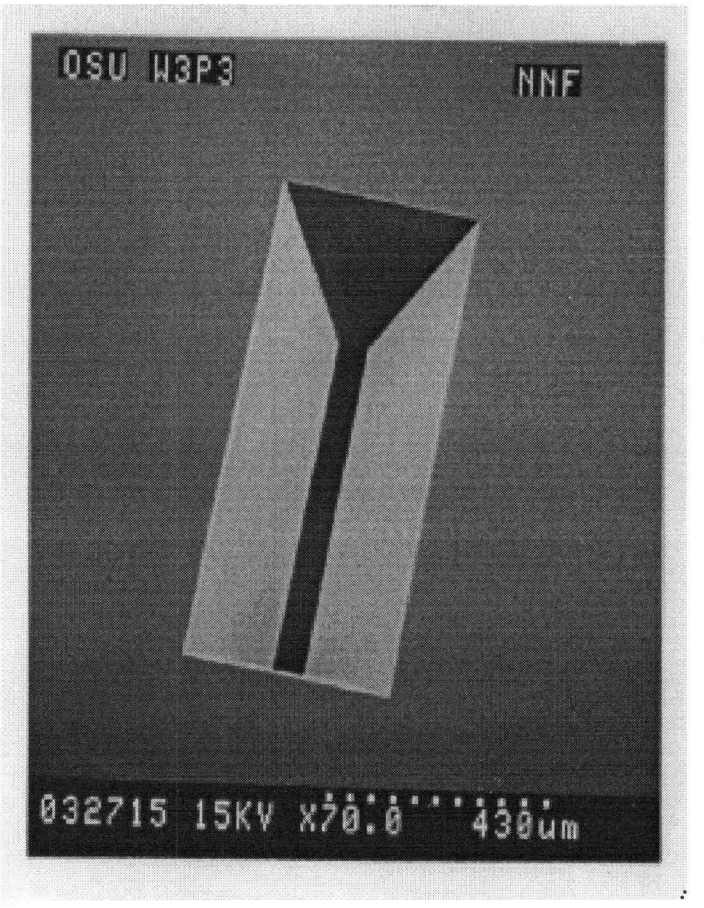

Fig. A.2. SEM micrograph showing the KOH etch along the <111> plane of the silicon wafer.

rotation calibration errors and variations in the height of the chip relative to the focal plane of the lens [Keith, *et al.*, 1991b]. Thermal drift problems can be reduced by using the largest possible current to minimize the e-beam writing time. To reduce stitching errors each grating was written using successive fields. The stitching errors, measured by writing verniers at the field boundaries, were typically no larger than 10 nm for adjacent fields and ~40 nm overall.

A charge density of 350 $\mu C/cm^2$ gave the proper exposure of the PMMA to yield gratings with an approximate 50% duty cycle. In the writing pattern the lines were undersized by 20 nm; this accounts for the beam size as well as exposure due to side scattering of the electrons. The pattern was also written over the edge of the windows to reduce the stress on the gratings.

After removal of the gold and developing the exposed PMMA the grating pattern is transferred to the nitride with an RIE process. RIE is a directional etch; the sample rests on the lower plate of a capacitor while the reaction gases are excited by RF to form a plasma. The ions are thus accelerated perpendicular to the sample and react with the surface layer. The grating etch called for CF_4 at 42 sccm and H_2 at 5 sccm with the chamber pressure of 15 mTorr and a DC bias of ~300 V. This will etch both the nitride and PMMA at ~25 nm min^{-1}; the nitride etch slows somewhat once the grating channels near completion so an etch time of ~5.5 minutes was used. The fabrication process is summarized in Fig. A.3.

Gratings with periods of both 250 nm and 500 nm were produced in both the 50 μm and 150 μm window widths. Since nitride wires of this size could not be made in the 0.5 mm or 1.0 mm lengths called for, all atom gratings had 1.5 μm horizontal support bars placed at 4 μm intervals. An SEM micrograph of a grating is shown in Fig. A.4.

Two larger windows for optical gratings were placed on each chip for the purpose of alignment and positioning feedback. Since the nitride was the same thickness as for the atom grating these

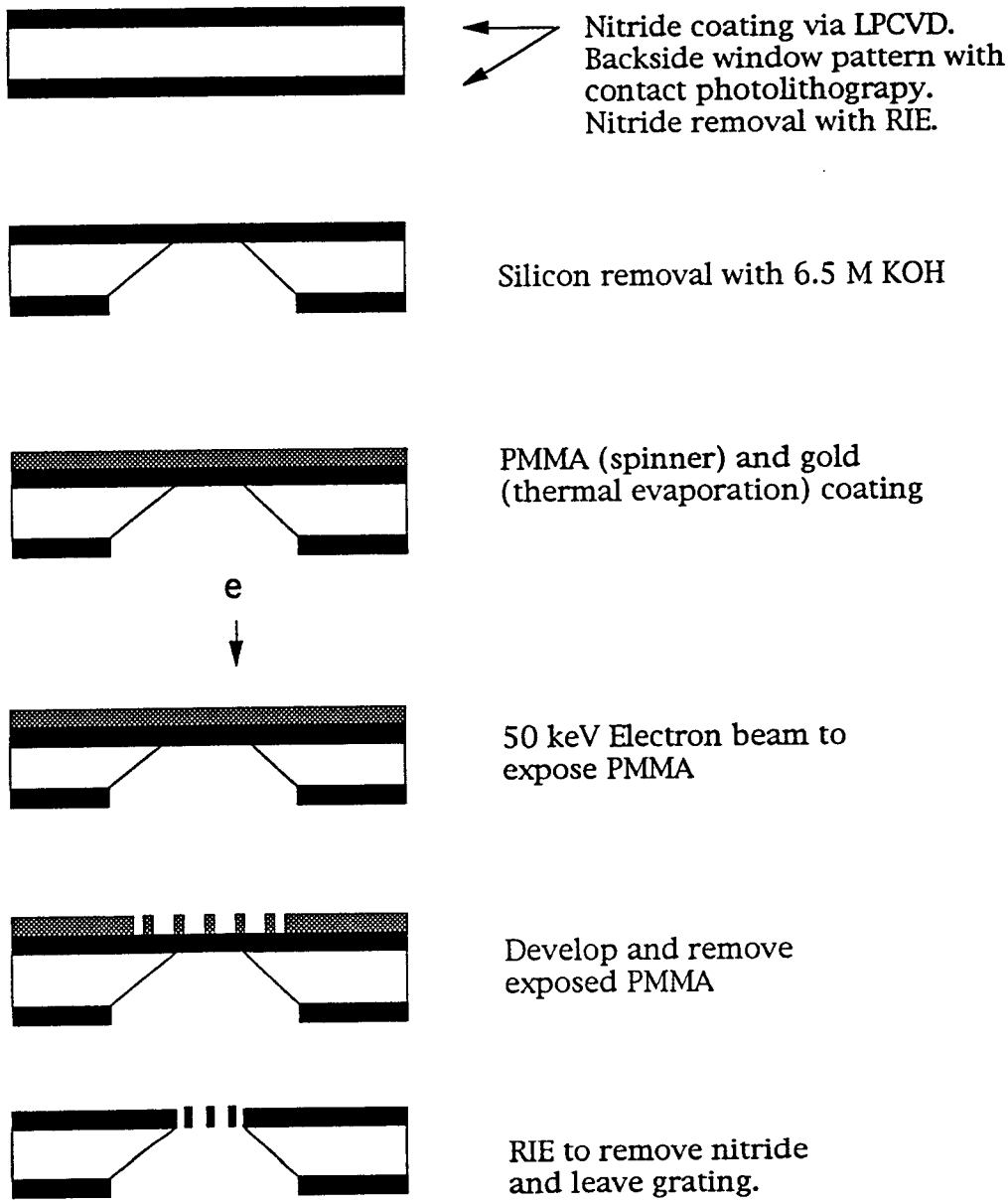

Fig. A.3. Grating Fabrication

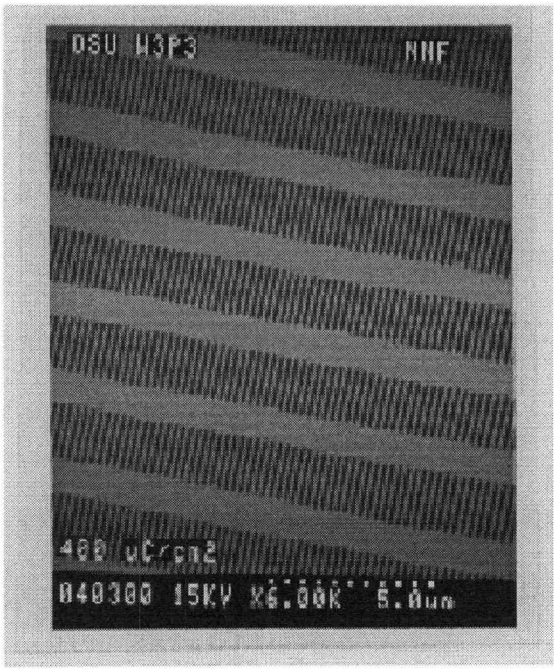

Fig. A.4. SEM micrograph of a free-standing silicon nitride grating. The grating spacing is 250 nm and the spacing of the horizontal support bars is 4 μm.

gratings were not very strong and usually broke during the RIE despite several designs to improve the strength of the gratings.

Appendix B
Rubidium Vapor Cell Construction

Many of the rubidium vapor cells used for spectroscopic applications were produced locally. A glassblower connected a 1 g Rb ampule to two empty glass cells (with optical quality windows) and a valve with a glass-to-metal seal. In the first attempt at making a vapor cell it was discovered that the rubidium does not tend to migrate across regions of metal so the rubidium must have a path from the ampule to the cells that does not include a glass-to-metal seal. This apparatus was connected to the oven section of the vacuum system and brought to ~10^{-7} torr with the turbomolecular pump.

Once the system has pumped down it is baked at 400 °C to remove possible contaminants from the tube and cell walls. This temperature is the suggested limit of heating for the glass-to-metal seal. The system, from ampule to cells, is wrapped first with flexible heater tape/wire and then with aluminum foil to give a more uniform temperature. The valve and glass-to-metal seal should not be covered with aluminum to keep this at a lower temperature. Bakeout should last at least 24 hours but a bakeout of longer than 48 hours is probably unnecessary.

The ampule's seal is broken while the vacuum system is isolated from the pumps since there is argon gas enclosed with the rubidium and the pressure in the chamber would rise above the turbomolecular pump safe operating pressure. Once the seal is

broken the glass encased metallic breaker is secured at the top of the ampule with a magnet which is fastened in place with a wrapping of wire. Bare metal breakers are not desirable due to possible contamination and reactions with the rubidium which can render the hyperfine structure undetectable from collisional broadening. The heater tape/wire and aluminum foil are rewrapped to expose the cells. The system is then heated to ~250-300 °C. The rubidium will diffuse from the ampule and collect in cold spots in the system. If the system is properly wrapped the bulk of the rubidium will collect in the cells and the tubes that lead to them. Any rubidium not in the cells can be moved by use of a heat gun. 24 to 48 hours should be enough time to move a sufficient amount of rubidium into the cells. There should be a large patch of the silver colored metal in the cells. Regions of transparent bluish metal are probably monolayers of rubidium and, by themselves, are insufficient for a good, long lasting vapor cell.

Prior to removal from the vacuum system any rubidium on the windows should be removed by gentle heating with a heat gun. Overheating may cause the rubidium to react with the glass and will reduce the available window space. Regions of brown and/or yellowish metal indicate a species of rubidium oxide or other contaminant and is indicative of overheating. The cells are removed by heating the connecting tubes with a natural gas torch. This is easier if the tubes have been "necked down" by the glassblower. When the glass softens it will collapse, due to the vacuum, and seal the tube on both ends. The cells should be wrapped in wet cloth to protect against heating from the torch.